



HAL
open science

Lateral variability of subtidal flow at the mid-reaches of a macrotidal estuary

Lauren Ross, Arnaldo Valle-Levinson, Aldo Sottolichio, Nicolas Huybrechts

► To cite this version:

Lauren Ross, Arnaldo Valle-Levinson, Aldo Sottolichio, Nicolas Huybrechts. Lateral variability of subtidal flow at the mid-reaches of a macrotidal estuary. *Journal of Geophysical Research. Oceans*, 2017, 122 (9), pp.7651-7673. 10.1002/2016JC012504 . insu-03678724

HAL Id: insu-03678724

<https://insu.hal.science/insu-03678724>

Submitted on 25 May 2022

HAL is a multi-disciplinary open access archive for the deposit and dissemination of scientific research documents, whether they are published or not. The documents may come from teaching and research institutions in France or abroad, or from public or private research centers.

L'archive ouverte pluridisciplinaire **HAL**, est destinée au dépôt et à la diffusion de documents scientifiques de niveau recherche, publiés ou non, émanant des établissements d'enseignement et de recherche français ou étrangers, des laboratoires publics ou privés.

Copyright

RESEARCH ARTICLE

10.1002/2016JC012504

Lateral variability of subtidal flow at the mid-reaches of a macrotidal estuary

Lauren Ross^{1,2} , Arnoldo Valle-Levinson³ , Aldo Sottolichio², and Nicolas Huybrechts^{4,5}

Key Points:

- Transverse distributions of tidal nonlinearities produce lateral variations of subtidal flow at the mid-reaches of a macrotidal estuary
- These tidal asymmetries are generated by different mechanisms from neap to spring tide
- For both neap and spring tide the sixth-diurnal (D6) overtide band in the current velocity was comparable to the quarter-diurnal (D4) band

Correspondence to:

L. Ross,
lauren.ross1@maine.edu

Citation:

Ross, L., A. Valle-Levinson, A. Sottolichio, and N. Huybrechts (2017), Lateral variability of subtidal flow at the mid-reaches of a macrotidal estuary, *J. Geophys. Res. Oceans*, 122, 7651–7673, doi:10.1002/2016JC012504.

Received 27 OCT 2016

Accepted 15 AUG 2017

Accepted article online 25 AUG 2017

Published online 21 SEP 2017

¹Department of Civil Engineering, University of Maine, Orono, Maine, USA, ²Laboratoire EPOC, University of Bordeaux, Pessac, France, ³Department of Coastal Engineering, University of Florida, Gainesville, Florida, USA, ⁴Sorbonne Universités, Université de Technologie de Compiègne, CNRS, Compiègne, France, ⁵Cerema, Direction Technique Eau, Mer et Fleuves, Margny Lés Compiègne, France

Abstract Transverse variations of tidal and subtidal flow were investigated in a macrotidal and convergent estuary. This was accomplished by combining data analysis of current velocities and water density with numerical modeling at the mid-reaches of the Gironde Estuary (France). Nonlinear mechanisms responsible for overtide generation and hence subtidal flows were found to vary across the estuary and from neap to spring tides. Subtidal flows were driven by a combination of internal asymmetry, tidal advective accelerations, nonlinear effects of water level variations, quadratic friction, and river discharge. The quarter-diurnal overtide band (D4) in the flow was generated by internal asymmetry and tidal advective accelerations during neap tide. The ratio of quarter-diurnal to squared semidiurnal bands ($D4/D2^2$) was largest (>0.3) in sections of the channel showing subtidal outflow. River discharge increased from neap to spring tides causing a subsequent increase of seaward subtidal currents. During spring tide, D4 was generated by tidal advective accelerations and quadratic friction combined with river discharge, rather than by internal asymmetry. The sixth-diurnal overtide (D6) in the flow was comparable to D4 for both neap and spring tides. Largest $D6/D2^3$ ratios were found in the shallowest cross-channel locations during both neap and spring tides.

1. Introduction

Subtidal, or tidally averaged, flows in estuaries can be driven by density gradients, wind, river discharge, or tidal nonlinearities (also referred to herein as tidal stresses, tidal rectification, or tidal distortion). Each of these mechanisms may exhibit the same order of magnitude and contribute to subtidal flows [Huijts *et al.*, 2009]. In particular, tidal rectification may produce spatial variations in the transverse distribution of subtidal flows, resulting from advective accelerations.

In addition to modifying subtidal flows, nonlinear advection also affects intratidal flows through flood-ebb asymmetries [Aubrey and Speer, 1985; Parker, 1991]. But these asymmetries, which are represented by overtides and compound tides, also result from bottom friction and tidal interactions with channel geometry, such as an along-estuary change in cross-sectional area [Tee, 1976; Aubrey and Speer, 1985]. In the absence of bottom friction, flood dominance (shorter and stronger flood currents) has been attributed to distortion of a nonreflected progressive tidal wave [Salomon and Allen, 1983; Dronkers, 1986; Parker, 1991]. In this case, a wave crest moves faster than the trough along the estuary. The crest of the tidal wave may partially overtake the trough, which yields a shorter and stronger flood and a longer and weaker ebb due to conservation of mass [Friedrichs and Aubrey, 1988]. This effect can be exaggerated during spring tides in the fortnightly tidal cycle (14.7 days) as the tidal range increases.

When considering the effects of bottom friction on tidal distortion, bottom stresses from estuary bathymetry are generally expressed as a nonlinear function [Uncles, 1981; Speer and Aubrey, 1985]. Bottom friction produces greater damping in shallow than in deep water, producing an earlier shift from flood to ebb tide at the sides of the estuary relative to the middle [Dyer, 1973; Valle-Levinson and Lwiza, 1995]. This time lag between low water at the mouth and low water in the inner estuary is greater than the lag at high water, resulting in a longer and weaker ebb and a shorter and stronger flood. As the tidal amplitude to depth ratio or distance into such an estuary increases, this effect should increase [Parker, 1991].

On the other hand, ebb dominance (shorter and stronger ebb currents) is caused by the weak exchange of water around high tide in estuaries with vast intertidal water storage areas and relatively deep channels. In

particular, at low tide, the intertidal areas are empty while channels remain completely submerged, which allows for a faster transition to flood. At high tide, the delay in the transition to ebb tide causes a relatively shorter ebb and strongest currents during the ebb. Ebb-dominant systems tend to flush sediments out-estuary and are more morphologically stable than flood-dominant systems [Friedrichs and Aubrey, 1988].

The manifestation of tidal distortion as asymmetries in the flood and ebb tide arise from specific nonlinear terms found in either the momentum or continuity equations governing the flow. A description of these nonlinear terms and how they generate overtides is needed to understand how tidal asymmetry and thus tidally induced subtidal flow is generated.

1.1. Overtide Generation

The estuaries of concern for this study are considered to be long and narrow, and so they have specific requirements for their characteristic length scales. The first requirement is that the depth, H , and the channel width, B , are both much less than the tidal wavelength, L_t ($H \ll L_t$ and $B \ll L_t$, respectively). Also, the ratio of the channel width to the barotropic Rossby Radius of Deformation, L_R , must be much less than the ratio of the tidal amplitude, A , over the depth ($B/L_R \ll A/H$). In systems that satisfy these requirements, the one-dimensional (along-channel) continuity and momentum equations can be derived as

$$\frac{\partial \zeta}{\partial t} + \frac{1}{b} \frac{\partial (h + \zeta) bu}{\partial x} = 0, \tag{1}$$

$$\frac{\partial u}{\partial t} + u \frac{\partial u}{\partial x} = -g \frac{\partial \zeta}{\partial x} - \alpha \frac{u|u|}{h + \zeta}, \tag{2}$$

where ζ is the water level elevation, u and h are the cross-sectionally averaged velocity and depth, respectively, g is gravitational acceleration, α is a drag coefficient, t is time, x is the along-estuary distance, and b is the width of the basin. The basin width, b , is described by an exponential function, $b(x) = \hat{b}e^{-x/L_b}$, in funnel-shaped estuaries where \hat{b} is the width at the mouth of the estuary and L_b is the e -folding length. The full derivation of these equations can be found in Parker [1991] and the references therein.

These equations contain three nonlinear terms, the advective acceleration term, $u \partial u / \partial x$ and the friction term, $\alpha(u|u|)/(h + \zeta)$, which are both from the momentum equation, as well as $\partial(\zeta bu) / \partial x$ from the continuity equation. The friction term can be split into two separate nonlinear mechanisms, $u|u|$, the quadratic friction term, and $\zeta u|u|$, which describes the effect of water elevation on momentum loss from friction [Parker, 1991; Godin, 1999].

The terms $\partial(\zeta bu) / \partial x$, $u \partial u / \partial x$, and $\zeta u|u|$ generate even harmonics like M4. In particular, the nonlinear continuity term $\partial(\zeta bu) / \partial x$ and the friction term $\zeta u|u|$ cause the crest of the tidal wave to travel faster than the trough due to the varying sea level, producing the asymmetric nature of M2 and generating even harmonics such as M4. The effect of the advective term $u \partial u / \partial x$ is also due to the crest of the wave having a larger celerity than the trough. However, this comes from the tidal current amplitude being comparable to the wave celerity in shallow systems. The influence of the advective term decreases with increased channel width convergence (smaller e -folding lengths), increased friction or a reflection of the tidal wave [Parker, 1991]. The quadratic friction term $u|u|$ can generate the same effect as the terms of the continuity and momentum equations (creating large M4/M2 ratios) when it is combined with a mean flow from river discharge. The quadratic friction term alone produces odd harmonics such as M6 [Prandle, 1991]. Momentum transfer to M6 through $u|u|$ decreases with increasing river discharge. However, as long as there are still slack tides, the quadratic friction term will generate M6. Similar processes to those described for M2 hold for other constituents such as S2 and N2. Also, when these constituents interact with each other, compound tides such as MS4 or MN6 can be formed.

The nonlinear terms described above transfer energy to higher harmonics (e.g., M4, M6, and M8) and produce asymmetric tidal velocities resulting in subtidal flows and a net transport of sediments [Dronkers, 1986; Speer and Aubrey, 1985; Friedrichs and Aubrey, 1988; Parker, 1991]. Estuaries tend to exhibit varying degrees of nonlinear response to tidal forcing as measured by the ratio of amplitudes of M4, M6, and M8 to M2 [Parker, 1991; Jay, 1991; Godin, 1999; Jay and Kukulka, 2003]. The most widely used indicator of nonlinearity is the M4/M2 ratio, which shows the effect of spectral energy transfer from M2 to M4. However, the ratio M6/M2 can also indicate nonlinearity as it represents energy transfer through frictional dissipation

[Aubrey and Speer, 1985; Blanton et al., 2002]. The ratio M_6/M_2 is typically smaller than the M_4/M_2 ratio. When the individual tidal harmonics cannot be resolved due to sampling frequency or duration [Foreman, 1977], the same ratios can be quantified for tidal species (or tidal bands). These tidal bands are denoted as D2, D4, and D6 for the semidiurnal, quarter-diurnal, and sixth-diurnal tidal species, respectively [Jay and Kukulka, 2003].

In addition to the barotropic tide generating asymmetries, other studies have looked into internal tidal asymmetry [Jay, 1991; Simpson et al., 1991; Jay and Musiak, 1996; Jay and Kukulka, 2003]. Internal asymmetry develops as the product of the time variations in both eddy viscosity and shear and results in internal overtides and a layered mean flow [Jay and Kukulka, 2003]. Since internal overtides produce zero vertically integrated flow they can be identified if the overtide phase shifts 180° over the water column (more details can be found in Jay and Kukulka [2003]). Jay and Kukulka [2003] found internal overtides (and internal tidal asymmetry) in the Columbia River Estuary where they reported a 180° phase shift in the D4 signal over the water column. Further, if the 180° phase shift occurs concurrently with an elevated normalized amplitude of the D4 overtide (quantified as D_4/D_2^2), the asymmetries are generated internally rather than through the barotropic tide. Internal asymmetry is often found during neap tides and periods of enhanced river runoff as enhanced tidal currents reduce water column stratification [Jay, 1991].

Studies have shown that tidal nonlinearities produce subtidal flows in estuarine systems [George and Simon, 1984; Speer and Aubrey, 1985; Parker, 1991; Jay, 1991; Godin, 1999; Jay and Kukulka, 2003; Gallo and Vinzon, 2005], but there is a lack of understanding how the transverse distribution of tidal nonlinearities affects lateral variations of subtidal flow. This study investigates the lateral distribution of subtidal circulation at the mid-reaches of the Gironde Estuary and its variability from neap to spring tides. This is the first study that examines lateral (depth-dependent) variability of subtidal flow in the Gironde. This system is macrotidal and hypersynchronous leading to its flood dominance and asymmetric tidal wave, ideal for studying tidal distortion as a driver of subtidal flow. There are two main goals of this study. The first is to determine whether transverse distributions of tidal nonlinearities produce lateral variations of subtidal flow. The second is to analyze how the lateral variations of tidal nonlinearities and subtidal flow patterns change from neap to spring tide. These objectives are accomplished using data analysis and numerical modeling. Most emphasis is on the data analysis, using numerical results to validate interpretations.

The remainder of this work will be presented as follows. The study area where field measurements were collected is presented in section 2. The methods used in this study including data collection, data analysis and numerical modeling will be presented in section 3 and the results are presented in section 4. Finally, the discussion and conclusions are presented in sections 5 and 6, respectively.

2. Study Area

The Gironde Estuary is a prototype of a macrotidal, funnel-shaped system. It is similar to other macrotidal and highly turbid estuaries (e.g., the Severn, the Ems, and the Loire), which makes this work relevant to other macrotidal and/or convergent systems. The mid-reaches of the estuary contain channels and small islands. However, the morphology becomes simpler in the downstream portions of the estuary, featuring a main channel (on the western side of estuary), a secondary channel known as Saintonge Channel (on the eastern side of the estuary) and a central shoal. The study area (Pauillac) was chosen as it is the first location downstream of Bordeaux without an island in the middle of the estuary, therefore enabling uninterrupted cross-channel measurements. The bathymetry of the Gironde varies from ~ 25 m deep at the deepest point of the mouth to 5–10 m in the upstream portions of the estuary and in the rivers (Figure 1b). The tide is predominantly semidiurnal with range between 2.5 and 5 m during the neap/spring cycle at the estuary mouth.

The Gironde is the largest estuary in Western Europe (Figure 1) with a surface area of approximately 635 km^2 and a tidal influence of approximately 180 km [Bonneton et al., 2015; Jalón-Rojas et al., 2015]. In terms of scaling, the Gironde is considered long and narrow and therefore is governed by equations (1) and (2) above. In particular, the narrow basin approximation ($B \ll L_t$) is satisfied since the maximum width of the system is 10 km (average width is 3 km) compared to an ~ 400 km tidal wavelength. The shallow water approximation holds ($H \ll L_t$) since the average depth is ~ 10 m. Finally, the ratio $B/L_R \ll A/H$ is also

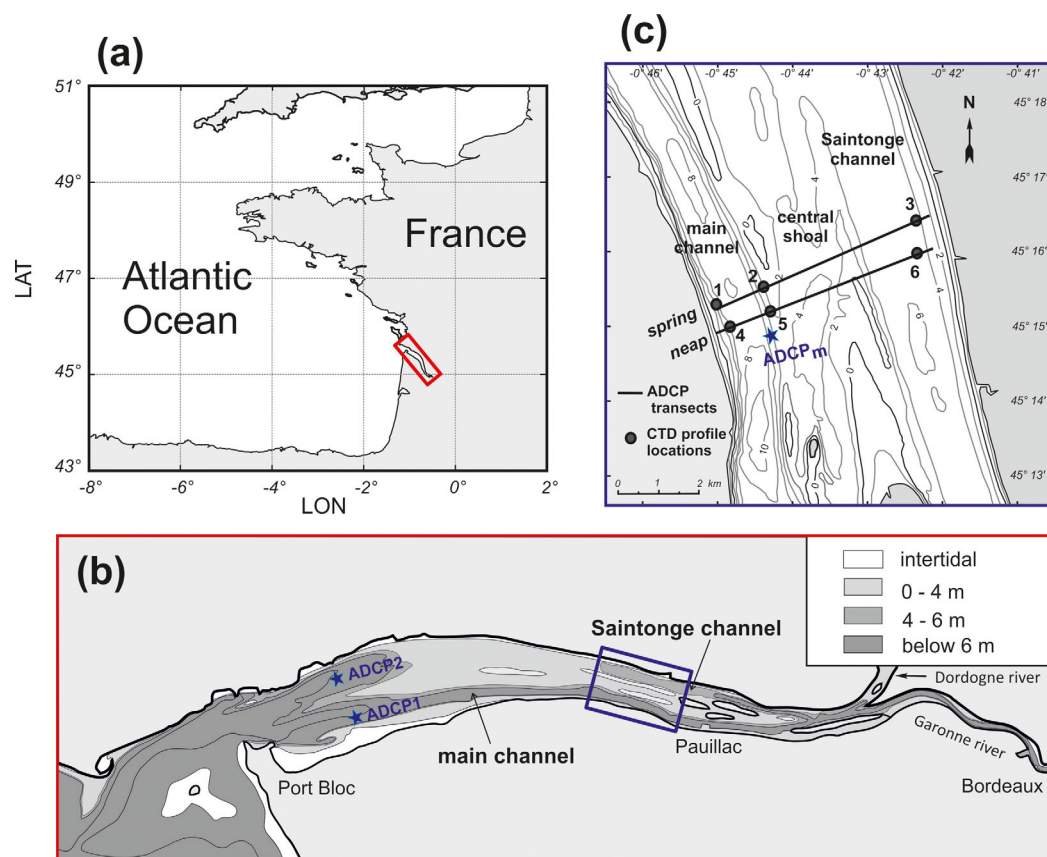


Figure 1. Study area map with (a) location in France, (b) zoom in on Gironde Estuary, depicting the location of two ADCP moorings (ADCP1 and ADCP2, deployed from June to November 2015) used for model validation. The blue square depicts the location of the ADCP transects and CTD casts performed in April 2015. (c) Zoom of ADCP transect location and CTD profile positions. The black lines depict the actual ADCP transect paths during spring and neap tides (the black line located upstream was the neap tide transect path). The black dots along the ADCP transect path depict the locations of the CTD profiles. During the spring tide sampling, the dot labeled 1 is for CTD profiles taken on the western shoal, 2 is for the main channel, and 3 is for the eastern shoal. Points 4, 5, and 6 are the same as 1, 2, and 3, but for the neap tide sampling.

fulfilled since the barotropic Rossby Radius, $L_R = \sqrt{gH}/f = \sim 99$ km, where f is the Coriolis parameter at 44° latitude and the tidal amplitude is at least $A = \sim 1.25$ m.

As the tide propagates into the Gironde friction increases and subsequently distorts the tidal wave as it continues upstream. In addition, the convergent width of the Gironde causes the tidal wave to amplify along the basin [Allen and Castaing, 1973; George and Simon, 1984; Ross and Sottolichio, 2016]. The tidal wave is nearly symmetric at the mouth of the estuary. However, as the tidal wave reaches Bordeaux (~ 100 km upstream), the estuary becomes flood-dominant with flood tide taking ~ 4 h and ebb tide about 8 h 25 min [Jalón-Rojas et al., 2015].

The estuary is also known for its high turbidity, which reaches approximately 10 g/L in the turbidity maximum zone [Sottolichio and Castaing, 1999; Sottolichio et al., 2011; Jalón-Rojas et al., 2015]. Sediment concentrations of several g/L and a grain size between 50 and 150 μm [Gibbs et al., 1989] at the surface present a challenge to measuring flow with acoustic methods because these methods are at the limit of their capability in such conditions [RD Instruments, 1999; Yorozuya et al., 2014]. This is problematic when attempting to obtain full water column velocity measurements using an acoustic device. The received acoustic signal is strongly attenuated in the water column by the ample backscattering from the suspended flocs, so the device will not record any velocity.

Two rivers, the Garonne and Dordogne, feed into the Gironde approximately 75 km upstream with a combined discharge varying depending on the season [Huybrechts et al., 2012]. Average discharge of the Garonne and Dordogne Rivers are highest during the winter and spring seasons (December–June) with

average combined (Garonne and Dordogne River) discharge reaching 2000 m³/s. During the winter and spring, the majority of the discharge originates from the Garonne River (Garonne winter average is ~750 m³/s while Dordogne average is ~400 m³/s). During the summer and fall months (July–November), average discharge values for the Garonne and Dordogne are approximately the same (~200 m³/s). The seasonal variations in river discharge can change the water column stratification in the estuary from well mixed during low discharge periods (summer and fall) to partially stratified during high discharge (winter and spring) [Allen *et al.*, 1980].

3. Methods

3.1. Data Collection

Both vessel-towed and bottom-mounted ADCPs were used to collect data in the Gironde Estuary during neap and spring tides in April 2015. Two 13 h experiments were performed during neap (14 April) and spring (20 April) tides across the Gironde Estuary near the town of Pauillac, located approximately 48 km from the mouth (Figure 1c). In addition, profiles of temperature and salinity were taken concurrently with the ADCP transects at three locations across the approximately 4.5 km transect (Figure 1c). The first profile was taken on the western shoal, the second in the main channel (approximately 1 km from the western shoal) and a third in the Saintonge Channel (or the eastern shoal, approximately 4.25 km from the western shoal). These profiles were obtained with an Optical Backscatter (OBS-3A; temperature accuracy: ±0.5°C, conductivity accuracy: 1%) probe and a Yellow Springs Instrument (YSI 6600 V2–4 Multi-Parameter Water Quality Sonde; temperature accuracy: 0.01°C, conductivity accuracy: 0.001–0.1 mS/cm) throughout the measurement period. A total of 12–13 profiles were obtained at each of the three stations during neap and spring tides.

Underway velocity profiles were recorded with a boat-mounted 1200 kHz RDI Workhorse ADCP in 50 cm bins at 120 pings per ensemble during one complete tidal cycle. Navigation was carried out with a Global Positioning System (GPS). A total of 12 transect repetitions were sampled for neap tides and 13 transects for spring tides. The transect data were organized in uniform grids across the estuary and with depth. The spring tide transect location was slightly further downstream (~500 m) than the neap tide transect. The transect had to be moved because of uncharted submerged pipe and rock barriers that became exposed in spring tides over the transect sampled at neaps. This resulted in a slight change in cross-channel bathymetry from one sampling period to the next, which will be detailed in the results section.

The ADCP data were trimmed before further data processing. Measurements within 10% of the bottom were excluded due to side lobe effects. In addition, any data ensemble with a signal return of less than 85% good data were omitted, which included 7% of the raw data. Further, error velocities greater than ~5% of the maximal flow were excluded, which included less than 1% of the raw data. A correction of the remaining data was then carried out following the method of Joyce [1989]. This correction involved a comparison of bottom track velocities measured by the instrument to instrument velocities derived by the GPS data.

Because of the high concentration of suspended sediment, the threshold acoustic contrast to identify the bottom had to be lowered for both neap and spring tides. As anticipated in section 2, data were lost in the main channel during the spring tide sampling due to the high turbidity, despite lowering the bottom detection threshold. It is estimated that ~6% of the flow went through the unsampled areas throughout the transect.

A second ADCP (RDI 1200 kHz), which will be referred to as ADCP_m, was moored (Figure 1c) to place the transect data in the context of temporal variability. This instrument was deployed in the main channel near the ADCP transect path for several days, encompassing the towed ADCP sampling period (Figure 1c). ADCP_m collected data in 0.25 m bins every 10 min. During neap tide, ADCP_m was moored at 45°16.326'N, 0°44.984'W from 12 to 14 April (~3 days) and for spring tide it was moored as close as possible to the location of the neap tide mooring, 45°16.248'N, 0°44.940'W from 19 to 20 April (~2 days).

Daily river discharge values from both the Garonne and Dordogne Rivers were collected from French governmental agencies (data available at www.hydro.eaufrance.fr) during the period 12–22 April 2015. Discharge measurements showed typical values for April with $Q_{\text{Garonne}} + Q_{\text{Dordogne}} = \sim 1050$ m³/s. There was some variation over the neap/spring cycle. In particular, the discharge was ~700 m³/s for the neap tide

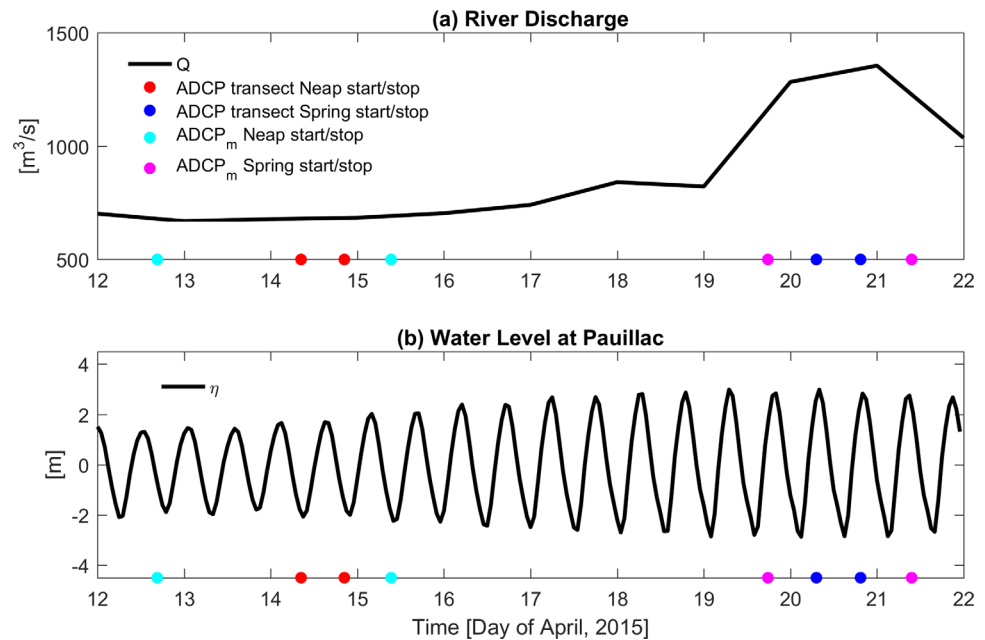


Figure 2. (a) River discharge (combined Garonne and Dordogne discharge) from 12 to 22 April 2015. (b) Water level elevations at Pauillac for the same time period as Figure 2a. The red dots on the x axis of Figures 2a and 2b depict the neap tide ADCP transect sampling start and stop times, the blue dots depict the spring tide ADCP sampling start and stop, the cyan dots represent the ADCP_m neap tide mooring start/stop times, and the magenta dots represent the ADCP_m spring tide mooring stop/stop times.

experiment and $\sim 1300 \text{ m}^3/\text{s}$ for the spring tide experiment (Figure 2a). Hourly water level measurements were collected from 12 to 22 April from a tide gage station located at the Pauillac harbor (data available at <http://maree.info/160>; Figure 2b).

3.2. Data Analysis

Instantaneous velocity data collected from both the neap and spring tide ADCP transects were interpolated to uniform grids of 0.5 m depth and 100 m length for a time period of ~ 13 h. The interpolated velocity data can be represented as the sum of multiple harmonics. The semidiurnal harmonic (period of ~ 12.42 h) and its first and second harmonic overtones, the quarter-diurnal (period of ~ 6.21 h) and the sixth diurnal (period of ~ 4.24 h), were separated from the subtidal signal of the observed flow using a sinusoidal least squares fit regression analysis [Lwiza *et al.*, 1991]. The analysis was performed independently on the time series generated at each grid point. The separate influence of the different semidiurnal components (M2, N2, and S2) could not be resolved because the period of observation fell short of the Rayleigh criterion [Foreman, 1977; Emery and Thomson, 2001]. Therefore, the tidal bands (or tidal species) rather than the proper harmonics M2, M4, and M6 were considered. The semidiurnal tidal band is referred to as D2, the quarter diurnal as D4, and the sixth diurnal as D6, where this notation has been adopted from Jay and Kukulka [2003]. The tidal flow was represented by the sum of a subtidal contribution plus a velocity amplitude and phase for each of the three tidal constituents (D2, D4, and D6). The subtidal signal includes the effects of diurnal tides, wind, density gradients, and tidal rectification. Further, the data collection took place for approximately 13 h, which was not long enough to resolve the diurnal tide. However, analysis of 100 days of water level measurements from the tide gage located in Pauillac revealed that the amplitude of the K1 and O1 harmonics, combined, account for $<2\%$ of the total tidal amplitude (not shown), indicating that the diurnal harmonics can be ignored without ambiguity.

In order to determine the transverse variations of subtidal flow the harmonic analysis was applied to the observed along-channel and cross-channel flow (u and v) collected from the ADCP transects for both spring and neap tides. This analysis included the three tidal species D2, D4, and D6 as follows,

$$u = u_o + A_{D2} \sin(\omega_{D2}t + \theta_{D2}) + A_{D4} \sin(\omega_{D4}t + \theta_{D4}) + A_{D6} \sin(\omega_{D6}t + \theta_{D6}), \quad (3)$$

where u_o is the subtidal velocity, t is time, A_{D2} , A_{D4} , and A_{D6} are the velocity amplitudes, ω_{D2} , ω_{D4} , and ω_{D6} are the harmonic frequencies, and θ_{D2} , θ_{D4} , and θ_{D6} are the velocity phases of the D2, D4, and D6

harmonics, respectively. Normalized ratios of the amplitudes of the D4 and D6 harmonics to the dominant D2 harmonic, adapted from *Jay and Kukulka* [2003], were calculated to check the strength of tidal nonlinearities at the mid-reaches of the estuary. The larger this ratio, the more likely that subtidal flows were a result of nonlinearities [*Friedrichs and Aubrey*, 1988]. A similar least squares fit was carried out for velocity measurements collected with ADCP_m and were compared to the transect data. The least squares fit regression analysis was applied to each depth bin (after conversion to sigma coordinates) of ADCP_m for the length of the sampling period (approximately six tidal cycles for neap and approximately four tidal cycles for spring, respectively).

In order to determine whether transverse variations of subtidal flow are generated by internal asymmetry or tidal advective accelerations (barotropic tide) the internal Tidal Froude Number was used [*Valle-Levinson and Schettini*, 2016]. Tidal advective accelerations, $u \partial u / \partial x$, can be scaled as U_o^2 / L_t where U_o is the tidal current amplitude and L_t is the tidal excursion. The baroclinic pressure gradient, or $\frac{g}{\rho} \frac{\partial \rho}{\partial x} h$ can be scaled as $\frac{g \Delta \rho H}{\rho L_t}$ or $\frac{g' H}{L_t}$, where g' is the reduced gravity. The internal Tidal Froude Number, or "Tidal Froude Number (Fr_o)" is the ratio of the scaled tidal advective accelerations to the scaled baroclinic pressure gradient (the length scale, L_t , cancels out),

$$Fr_o = U_o^2 / (g' H). \tag{4}$$

This ratio is used to determine the role of the baroclinicity in the subtidal flow. For this comparison, U_o was calculated as the depth-averaged D2 tidal velocity amplitude from the harmonic analysis. The average cross-channel depth is H and the angled brackets denote a tidal average. The reduced gravity was calculated as $g' = \frac{g \Delta \rho}{\rho}$, where $\Delta \rho$ was quantified in two ways. First, it was calculated using a cross-sectional average of the density profiles collected using the OBS-3A and YSI probes. This approach produced values of the Tidal Froude Number across the estuary, hence it reflects cross-channel density gradients ($\Delta \rho = \frac{\partial \rho}{\partial y} \Delta y$; Figure 4). Second, it was calculated from density profiles collected at each of the three observation stations throughout the tidal cycle ($\Delta \rho = \frac{\partial \rho}{\partial z} \Delta z$). This approach produced values of the Tidal Froude Number considering vertical variations in density. The depth profile was obtained from the ADCP's bottom track.

Values of Fr_o greater than 1 ($\log_{10}(Fr_o) > 0$) implied that tidal advective accelerations were more influential in driving the subtidal flow than baroclinic pressure gradients. On the other hand, Fr_o less than 1 ($\log_{10}(Fr_o) < 0$) indicated that the subtidal flow was influenced more by density gradients than advective accelerations. Values near 1 show the influence of both tidal advective accelerations and pressure gradient in driving subtidal flow. It is assumed that a Fr_o greater than 1.25 ($\log_{10}(Fr_o) > 0.1$) indicates that advective accelerations dominate over the baroclinic pressure gradient and values less than 0.75 ($\log_{10}(Fr_o) < -0.1$) indicate that the baroclinic pressure gradients dominate [*Valle-Levinson and Schettini*, 2016].

3.3. Numerical Model

Numerical computations were used to complement results derived from data analysis. In particular, the model helped to verify the forcing mechanisms of the observed along-channel subtidal flow. Simulations were performed with the Telemac 3D finite-element system, which has modeled various estuarine configurations [*Brown and Davies*, 2010; *Huybrechts et al.*, 2012]. The model domain was used by *Huybrechts et al.* [2012] to optimize two-dimensional hydrodynamic modeling (tide and currents) in the Gironde using Telemac 2D. *Huybrechts et al.* [2012] only considered depth-averaged flow so a slightly modified unstructured grid was implemented for this study of three-dimensional currents. The grid is comprised of 10 vertical layers that each contains 47,646 nodes. Forcing for the Telemac 3D model included daily river discharge measurements at upstream boundaries and 42 tidal harmonics at the downstream boundary at a 30 s time step. The inclusion of 42 harmonics produced a more realistic water level variation than the simplified harmonic analysis that only included three harmonics. Therefore, the model results were subjected to the same harmonic analysis that was applied to these data, which produced similar results.

Simulated tidal levels were validated by using tide gage records from 9 stations located along the Gironde Estuary and the Garonne River (Figure 1b and Table 1). Root mean square errors (RMSE) and normalized root mean square errors (NRMSE or the RMSE divided by the range of the measured data) between model results and tide gage data are detailed in Table 1. Model results were most accurate near the mouth of the estuary (Port Bloc, RMSE of 0.08 m; Table 1). Near the river confluence zone (Le Marquis; Table 1) and at the

Table 1. Root-Mean-Square Errors (RMSE) and Normalized Root-Mean-Square Errors (NRMSE) for Model Validation With the Tidal Amplitude at Nine Tide Gage Stations Along the Gironde

Location	Distance From Mouth (km)	RMSE (m)	NRMSE (%)
Port Bloc	0	0.0	1.6
Richard	16	0.13	2.6
Lamena	32	0.09	1.8
Pauillac	49	0.11	2.2
Fort Medoc	59	0.09	1.8
Ambes	70	0.11	2.2
Le Marquis	79	0.13	2.6
Bassens	87	0.12	2.4
Bordeaux	93	0.12	2.4

tide gage station Richard, the error increased to 0.13 m. These values are comparable to *Huybrechts et al.* [2012] and are low enough to consider the validation as satisfactory.

Velocity validation in the Gironde was accomplished by using two ADCP moorings located ~20 km downstream of the study site, which collected data for 6 months. These data were chosen for model validation due to the length of the time series, which covered both spring and neap tides as well as seasonal variations. To the best of the authors knowledge, no other long-term ADCP measurements are available at this time. Figure 3

shows a comparison of bottom and surface currents from the two ADCPs (ADCP1 and ADCP2 in Figure 1b) compared with model output for 10 days in 2015. Values of RMSE are presented in Table 2 for each ADCP during neap tide, spring tide, and for the entire sampling period. In addition, the NRMSE is detailed in Table 2. The RMSE was under 14 cm/s for both neap and spring tide velocity simulations producing a NRMSE value of 8.9%. The results at the location of ADCP 2 (Figure 1c) were more accurate than that of ADCP 1 (maximum NRMSE of 6.25% for ADCP 2 and 8.9% for ADCP 1). This could be attributed to dredging activities that take place year round in the main channel of the Gironde (location of ADCP 1) resulting in a different bathymetric profile than the model mesh.

4. Results

This section describes salinity, tide and river discharge variations throughout the sampling period. Next, the transverse variations of subtidal flow and tidal nonlinearities from the vessel towed ADCPs are discussed. All figures of tidal and subtidal flow are oriented looking out-estuary with negative values (cool colors) depicting outflow and positive values (warm colors) depicting inflow. The ADCP mooring data ($ADCP_m$) is then considered to verify the presence of tidal nonlinearities found in the ADCP transect data. Finally, numerical model simulations are examined to help determine subtidal flow drivers.

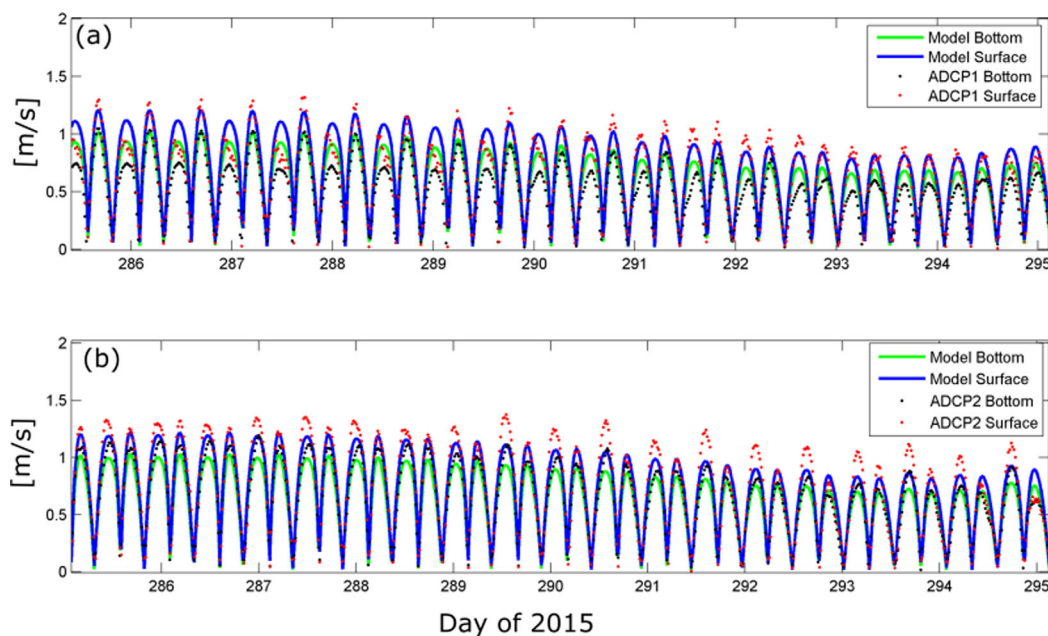


Figure 3. Validation of 3-D current speed (m/s) from the Telemac 3D model. (a) Model output at the surface (blue) and bottom (green) compared to ADCP1 data at the surface (red dots) and bottom (black dots). (b) Same as Figure 3a but for ADCP2.

Table 2. Root-Mean-Square Errors (RMSE) and Normalized Root-Mean-Square Errors (NRMSE) Between Model Simulation Results of Current Magnitude and Data From ADCP1 and ADCP2

			RMSE (m/s)	NRMSE (%)
ADCP1	Surface	All	0.13	8.2
		Neap	0.09	5.7
		Spring	0.14	8.9
	Bottom	All	0.13	8.2
		Neap	0.12	7.6
		Spring	0.14	8.9
ADCP2	Surface	All	0.10	6.25
		Neap	0.10	6.25
		Spring	0.08	5.0
	Bottom	All	0.08	5.0
		Neap	0.07	4.4
		Spring	0.08	5

4.1. Salinity

Salinity variations over a tidal cycle follow an expected pattern over both the shoals and the channel, with salinity increasing during flood and decreasing during ebb. Weak vertical salinity gradients were found during neap tide for the first 3.6 h (day 14.25 to 14.4 of April) of sampling. This was representative of the end of ebb-early flood, with values ranging from 0 g/kg at the surface to a max of 2 g/kg at depth in the main channel (Figures 4a–4c). Increased vertical salinity gradients when found at the end of flood (time 14.4 to 14.5), when salinity increased rapidly from 2 to 7 g/kg throughout most of the water column (Figures 4a–4c). Overall, during

neap tide the water column was weakly stratified across the estuary during flood tide and was fully mixed (fresh) during ebb. Similar results were found for salinity during spring tide, but with an increase in the maximum values at each sampling location (e.g., maximum salinity for spring tide was 10 g/kg in the main channel; Figures 4d–4f).

The bottom 2 m of each flood-tide profile indicated decreased salinities relative to the surface. This could be caused by reduced conductivity from increased suspended sediment concentration. During slack tides (especially on neaps) in the Gironde, the settling of suspended sediments leads to the formation of a high concentration layer near the bed (i.e., a layer of fluid mud) [Dyer, 1986]. This layer of fluid mud can interfere with the instruments capability to correctly measure conductivity [Le Hir et al., 2000; Sottolichio,

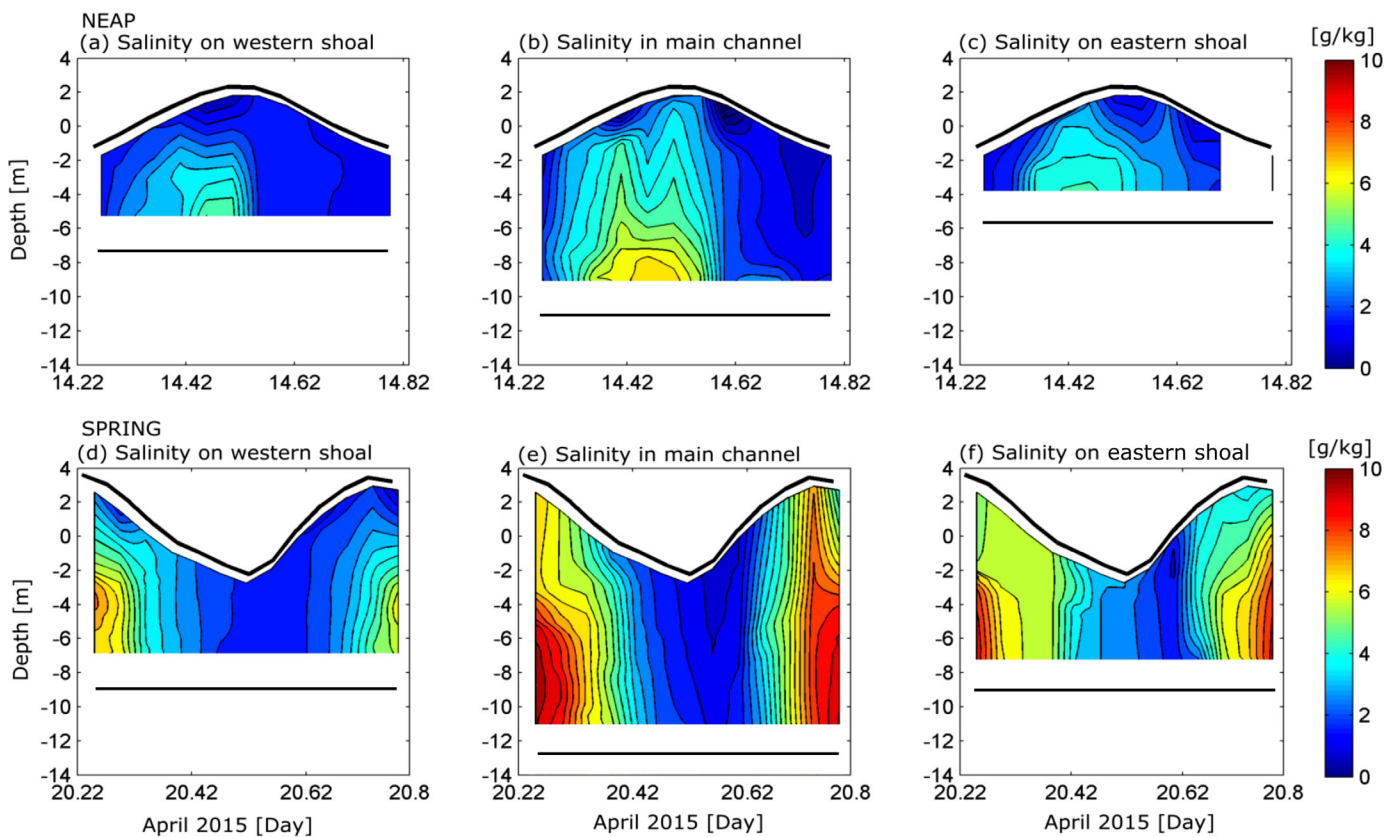


Figure 4. Time series of salinity profiles (g/kg) during neap tide at (a) the western shoal, (b) the main channel, and (c) the eastern shoal. The black line at the top of each subplot depicts the water surface while the black line at the bottom depicts the approximate location of the bottom. (d–f) Same as Figures 4a–4c, but during spring tide.

1999]. Another potential cause of the salinity reduction can be explained by sediment-induced stratification in the turbidity maximum zone, which has been found to occur in highly turbid systems [Geyer, 1993; Talke *et al.*, 2009; Becker and Winter, 2016]. In particular, the TMZ retains low salinity water as higher salinity water is advected over [Becker and Winter, 2016]. In the current work, suspended sediment concentrations were not collected and so the instruments were not calibrated to quantify these concentrations. The bottom 2 m of each profile was hence removed because of the unknown cause of the near-bottom salinity decrease.

4.2. Tide Propagation

Water level variations at Pauillac showed increasing tidal asymmetry (flood dominance) from neap (12–14 April) to spring (19–22 April) tides (Figure 2b). The D2 harmonic and its first overtones, D4 and D6, were investigated in order to quantify the extent of the nonlinearities. From neap to spring tide the amplitude of the D2 harmonic increased nearly 1 m (from 1.75 to 2.68 m), while the phase changed negligibly (from 66° to 61°). This increase in tidal amplitude led to a subsequent increase in tidal asymmetry from neap to spring tide, which could be compounded with an increase in river discharge (Figure 2a). In particular, the tidal nonlinearity ratios (phases) varied from $D4/D2 = 0.03$ ($2D2-D4 = 88^\circ$) and $D6/D2 = 0.04$ ($3D2-D6 = 59^\circ$) to $D4/D2 = 0.12$ ($2D2-D4 = 11^\circ$) and $D6/D2 = 0.07$ ($3D2-D6 = 89^\circ$) from neap to spring tide, respectively. For neap tides, the amplitude and phase of the M2 harmonic were 1.75 m and 66°, respectively. The tidal nonlinearity ratios were $M4/M2 = 0.03$ and $M6/M2 = 0.04$ with respective phases of $2M2-M4 = 88^\circ$ and $3M2-M6 = 59^\circ$. For spring tides, the M2 amplitude and phase was 2.68 m and 61°, respectively. The nonlinearity ratios were $M4/M2 = 0.12$ and $M6/M2 = 0.07$ with phases of $2M2-M4 = 11^\circ$ and $3M2-M6 = 89^\circ$. The phase calculations ($2D2-D4 = 88^\circ$ and 11° from neap and spring tides) indicate that the Gironde is a flood-dominant system, as expected [Allen *et al.*, 1980; Friedrichs and Aubrey, 1988]. The larger amplitude ratios during spring tides indicate that the tidal wave becomes more asymmetric as the water level increases. The elevated $D6/D2$ amplitude ratio suggests that quadratic friction increases during spring tides. The effect of tidal nonlinearities on transverse subtidal flow is discussed next.

4.3. Neap Tide

Neap tide (14 April) subtidal circulation and tidal species amplitudes (D2, D4, and D6) were quantified at the mid-reaches of the estuary for both along and cross-channel flows. Along-channel subtidal flow was laterally sheared showing complex cross-channel patterns (Figure 5a). The along-channel flow showed outflow in the main channel (0.5–1.25 km; >0.5 m/s), at the confluence of the central shoal and Saintonge Channel (2.2–2.6 km; ~ 0.25 m/s) and at the eastern edge of the Saintonge Channel (3.75–4.75 km; ~ 0.15 m/s) (Figure 5a). Weak inflow (-0.2 m/s) was found to be laterally sheared next to regions of strong outflow (>0.5 m/s). In particular, inflow was -0.15 m/s from 1.6 to 2.2 km and -0.25 m/s from 2.6 to 3.75 km. Cross-channel subtidal flow ranged from approximately -0.1 to 0.1 m/s over the channel width (Figure 5b). Since the subtidal cross-channel flows are $\sim 20\%$ of the along-channel subtidal flow, both components will be considered when calculating the amplitudes of the tidal bands D2, D4, and D6. Semi-diurnal tidal current amplitude showed strongest velocities in the main channel (0.5–1.8 km; >2 m/s) and on the eastern side of the estuary (3.5–4.75 km; ~ 1.8 m/s) (Figure 5c). D2 current amplitudes decreased over the sharp bathymetric changes in the middle of the estuary that formed the central shoal (from 1.5 to 2.3 km).

In order to determine the effect of nonlinearities on the transverse variations of subtidal flow, the duration of flood and ebb tide and the amplitudes of the D4 and D6 tidal bands were compared to that of the squared and cubed D2 amplitude, respectively. The duration of flood and ebb tide were calculated as the total number of hours that the tidal flow was directed out-estuary (ebb duration) and into the estuary (flood duration). During neap tides, the main channel (0.5–1.5 km) and the central shoal (2.1–2.4 km) were flood dominant while the estuary was ebb-dominant elsewhere (Figure 6a).

Cross-channel locations with elevated $D4/D2^2$ ratios are observed where the estuary is flood dominant and exhibits subtidal outflow (Figures 6a and 6b). Elevated $D4/D2^2$ ratios (>0.2) are in the main channel (0.5–1.3 km), at the confluence of the central shoal and the Saintonge Channel (2.2–2.75 km), and at the eastern edge of the Saintonge Channel (4–4.3 km) (Figure 6b). Lowest values of $D4/D2^2$ (close to 0) were found where the subtidal flow was landward (1.5–2 and 2.8–3.8 km) and the estuary was ebb dominant.

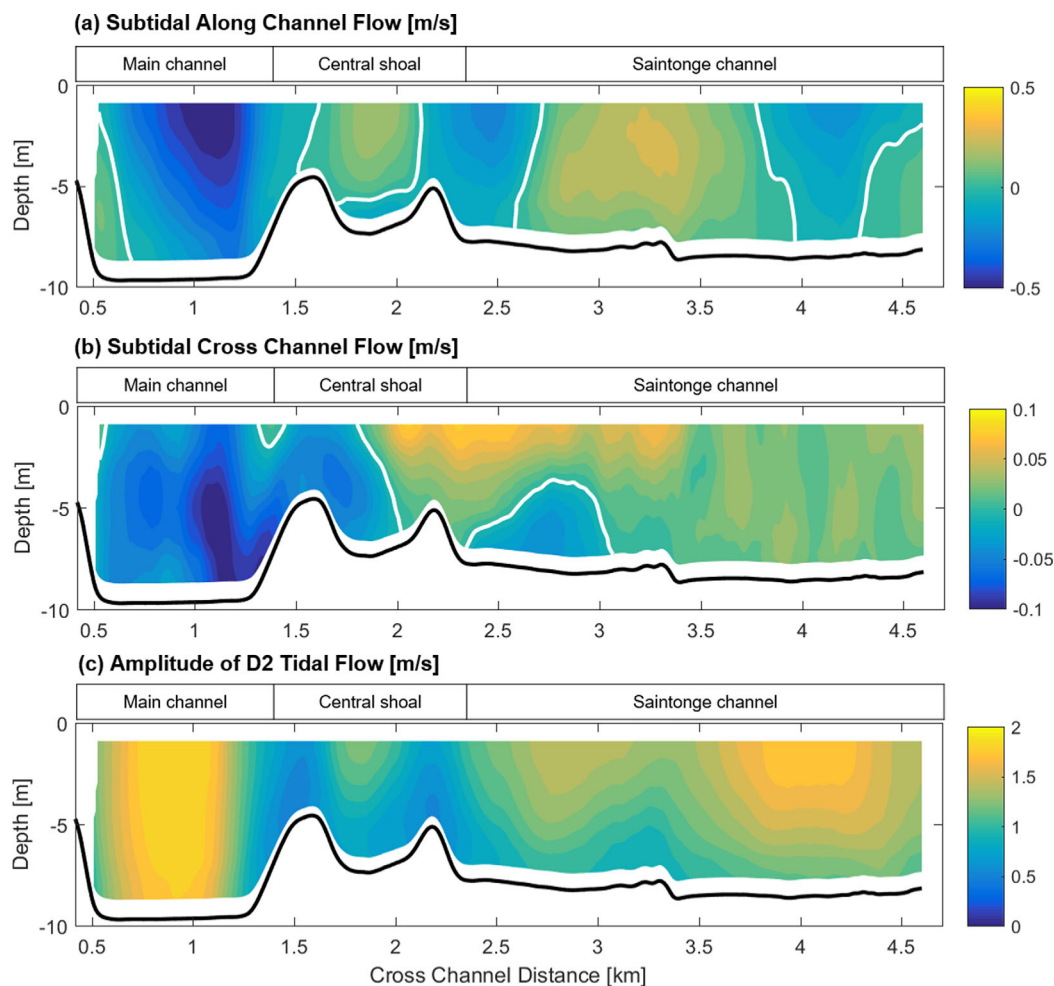


Figure 5. (a) Along-channel subtidal velocity (m/s) during neap tide calculated from the least squares fit analysis. The x axis depicts cross-channel location with $x = 0.5$ being the western portion of the main channel and $x = 4.5$ being the eastern side of the estuary (Saintonge Channel). Outflow is depicted by negative values. (b) Same as Figure 5a but for cross-channel subtidal velocity. (c) The amplitude of the semidiurnal (D2) tidal band during neap tide.

The largest D_6/D_2^3 ratio was observed in regions with negligible or small subtidal flow and weak D_4/D_2^2 ratios (<0.1) indicating that in these areas energy from D2 is passed to D6 through quadratic friction instead of to D4 (Figure 6c). For example, D_6/D_2^3 reached ~ 0.5 over the center shoal (particularly at the shallowest region, at 1.5 km). In the Saintonge Channel (2.8–3.8 km), the D_6 to D_2^3 ratio was >0.25 in regions of subtidal inflow (Figure 6c). Comparing the D_4/D_2^2 and D_6/D_2^3 ratios to subtidal flows indicate that transverse distributions of tidal nonlinearities produce lateral variations of subtidal flow during neap tide.

One method to determine if the nonlinearities are generated by internal asymmetries or barotropic asymmetries is to investigate the phase of the D4 amplitude over the water column. If the D4 internal overtide is present, its phase will vary by approximately 180° over the water column due to zero vertically integrated transport throughout the tidal cycle [Jay and Musiak, 1996; Jay and Kukulka, 2003]. A phase shift of 180° over the water column is found in D4 between 2.3 and 2.8 and 3.3–3.6 km (Figures 6d and 6e). The 180° phase shift that occurs from the central shoal to the Saintonge Channel (2.3–2.8 km) is in the same cross-channel location as the largest D_4/D_2^2 ratio (>0.3 ; Figure 6b), indicating that tidal nonlinearities are likely linked to internal asymmetry in this section of the channel. The phase of D6 is also shown for completeness, however, internal asymmetry is generally considered to cause quadratic nonlinearities in the vertical momentum and therefore is only expected to generate even overtides and a mean flow [Jay and Musiak, 1996]. These findings are now compared to spring tides.

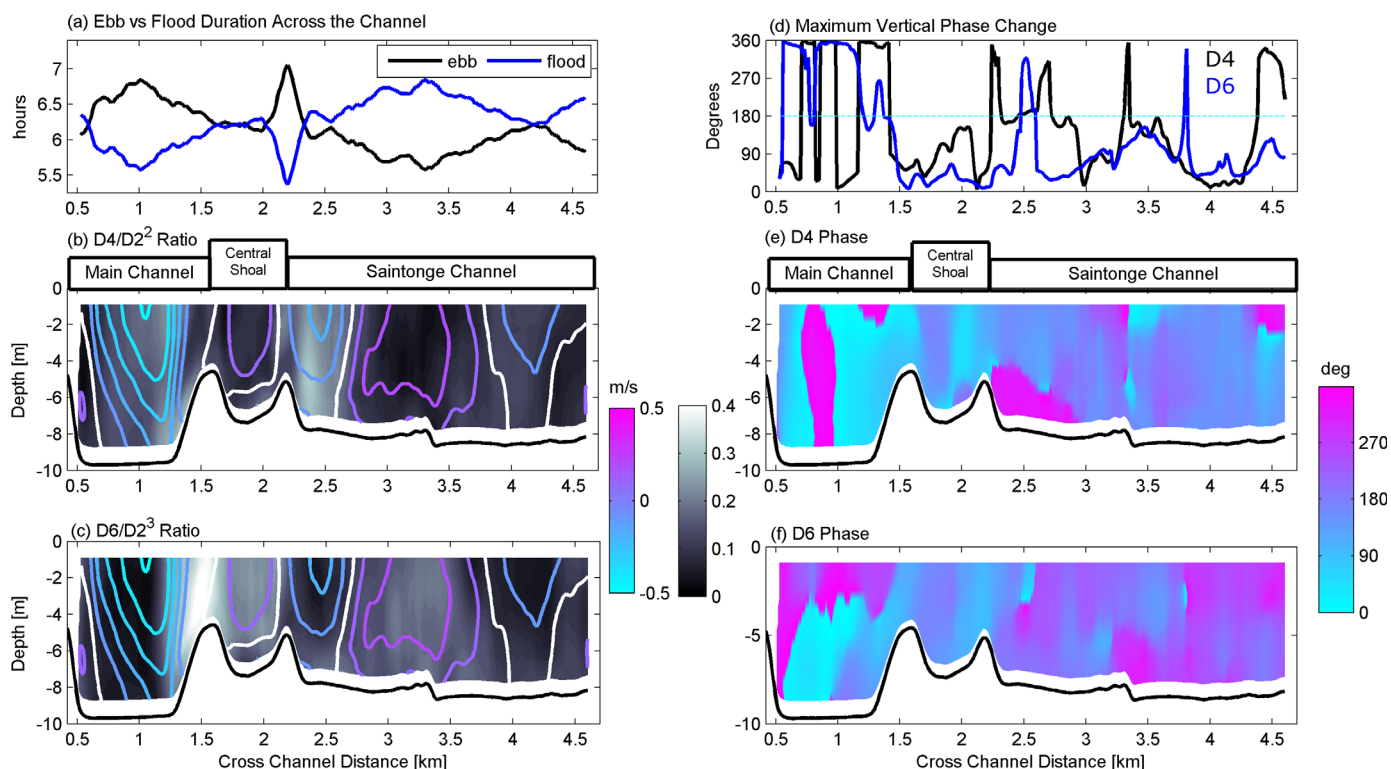


Figure 6. Neap tide (a) flood and ebb duration in hours with respect to cross-channel distance (x axis). Ratio of (b) $D4/D2^2$ current velocity amplitudes and (c) $D6/D2^3$ current velocity amplitudes for neap tides with respect to cross-channel location. (d) Maximum vertical phase change difference from D4 and D6 with respect to cross-channel location. Phase of (e) D4 and (f) D6 with respect to cross-channel location.

4.4. Spring Tide

Spring tide (20 April) subtidal circulation and tidal species amplitudes and phases were compared to those of neap tide. The subtidal flow pattern was similar to that of neap tide, but was overall much weaker (reaching ~ 0.4 m/s during neap and only ~ 0.1 m/s during spring tide) and subtidal outflow was found to dominate across the estuary (Figures 5a and 7a). The strongest along-channel subtidal flows were found on the eastern side of the main channel (1.3–1.5 km; >50 cm/s), in the center shoal (1.8–2.75 km; ~ 25 cm/s), and in the Saintonge Channel (4.4–4.9 km; ~ 30 cm/s), and in all cases were directed seaward (Figure 7a). Only three regions of subtidal inflow were found in the along-channel subtidal flow. These were on the western side of the main channel (0.75–1 km and from mid water column to the bottom), over the central shoal (1.6–1.8 km), and in Saintonge Channel (2.6–2.4 km) (Figure 7a). Subtidal cross-channel flow reached -0.15 m/s near the surface in the Saintonge Channel (Figure 5b). The cross-channel subtidal flow was primarily directed toward Saintonge Channel (to the east, Figure 1). The eastward lateral subtidal flows could be caused by increased river discharge during spring tides combined with curvature effects and Coriolis acceleration.

The semidiurnal tidal current amplitude was strongest in the Saintonge Channel (3.5–4.75 km; ~ 2 m/s). Further, the D2 amplitude diminished at locations with shallowest depths, namely between 1.5 and 2 and 3.2 and 3.4 km but also in the main channel between 0.75 and 1.2 km (Figure 7c). Excessive turbidity on the western portion of the main channel hindered collection of ADCP data during the spring tide sampling (estimated that $\sim 6\%$ of the total flow was lost). This channel portion could not be included in the analysis.

During spring tide generation of the D4 and D6 harmonics was more pronounced than during neap tide (Figure 8). The channel displayed flood dominance (ebb duration exceeded that of flood) over the entire channel cross-section (Figure 8a). The $D4/D2^2$ ratio showed highest values (~ 0.5 s/m) in the main channel where the difference between flood and ebb duration was most pronounced (0.75–1.75 km; Figures 8a and 8b). Other cross-channel locations where $D4/D2^2 > 0$ were the central shoal (2.75–3.4 km; ~ 0.3) and the Saintonge Channel (4–4.8 km; ~ 0.25) (Figure 8b). During neap tides, the cross-channel sections with highest

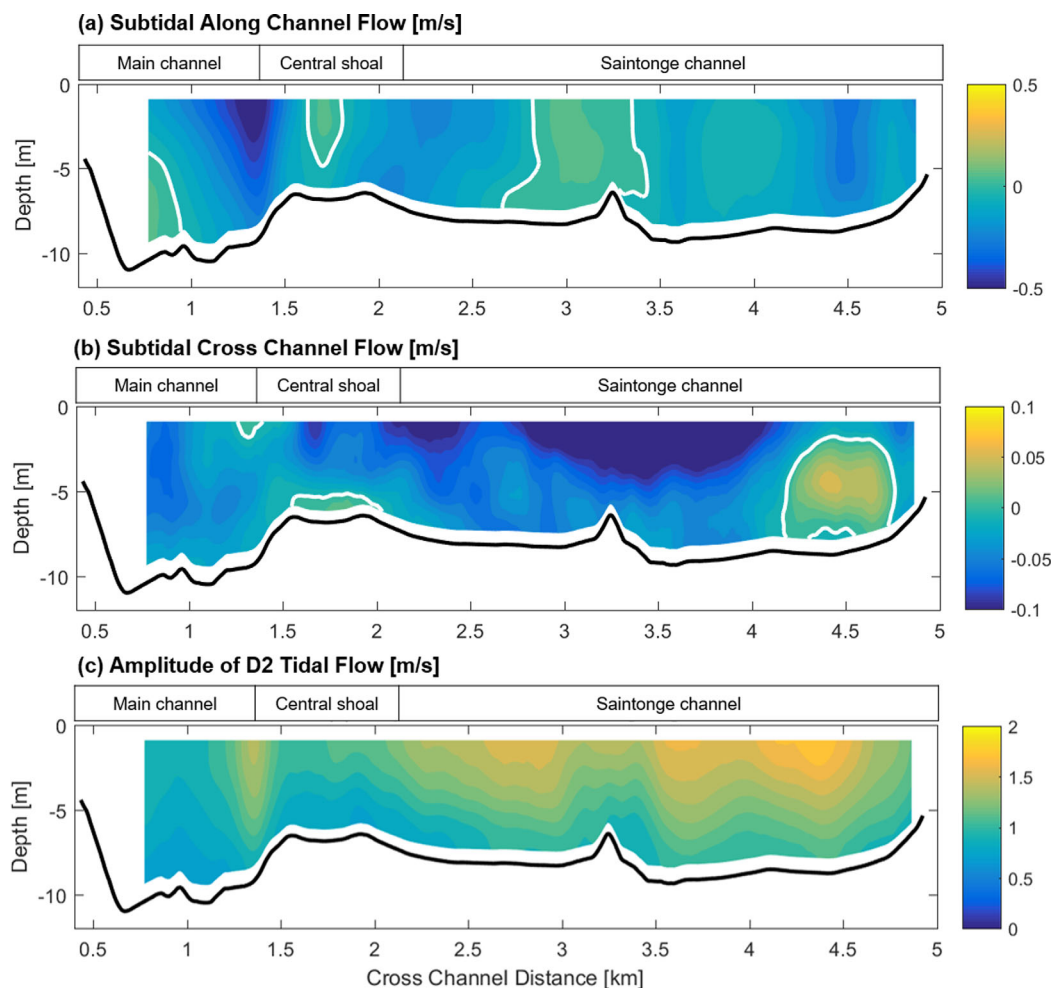


Figure 7. Same as Figure 5 but for spring tides.

$D4/D2^2$ ratios coincided with sites of along-channel subtidal outflow (Figure 6b), however, there was no such pattern during spring tides (Figure 8b). The $D6/D2^3$ ratio showed values >0 in the main channel (from 0.75 to 1 km), in the Saintonge Channel (from 3 to 5 km), and largest values (~ 0.45) over the central shoal (from 1.5 to 2.5 km) (Figure 8c).

The phase change over the water column was investigated for the D4 overtide to determine if its generation mechanism was internal asymmetry or tidal asymmetries. The few cross-channel locations showing a 180° phase shift over the water column for the D4 overtide did not occur concurrently with locations where $D4/D2^2 > 0$ (Figures 8b, 8d and 8e). This indicates that the D4 overtide was generated by tidal asymmetries rather than internal asymmetries during spring tides. To verify that the tidal nonlinearities found in the ADCP transect data are found in longer time series, the moored ADCP data ($ADCP_m$) is now investigated.

4.5. Moorings: $ADCP_m$

Tidal nonlinearities were also examined with $ADCP_m$ to complement the findings from the ADCP transects (Figure 9). For ease of data processing and visualization, the velocities are shown in sigma-coordinates for depth, where 0 is the surface and -1 is the location of the first $ADCP_m$ bin (1.54 m above the bottom). The amplitude of the D2, D4, and D6 tidal species as well as the nonlinearity ratios, $D4/D2$ and $D6/D2$ were calculated for both neap and spring tides. The amplitude of D4 (maximum of 0.28 m/s at the surface) was larger than D6 (maximum of 0.14 m/s) throughout the water column during neap tide (Figure 9b). The amplitude of D2 ranged from ~ 1.5 m/s at the surface ($z/H=0$) and decreased monotonically to 1.2 m/s at the location of the first ADCP bin ($z/H=-1$) (Figure 9c). The $D4/D2$ ratio was larger than the $D6/D2$ ratio over the water column during neap tide (Figure 9b) and the phase of both D4 and D6 remained constant

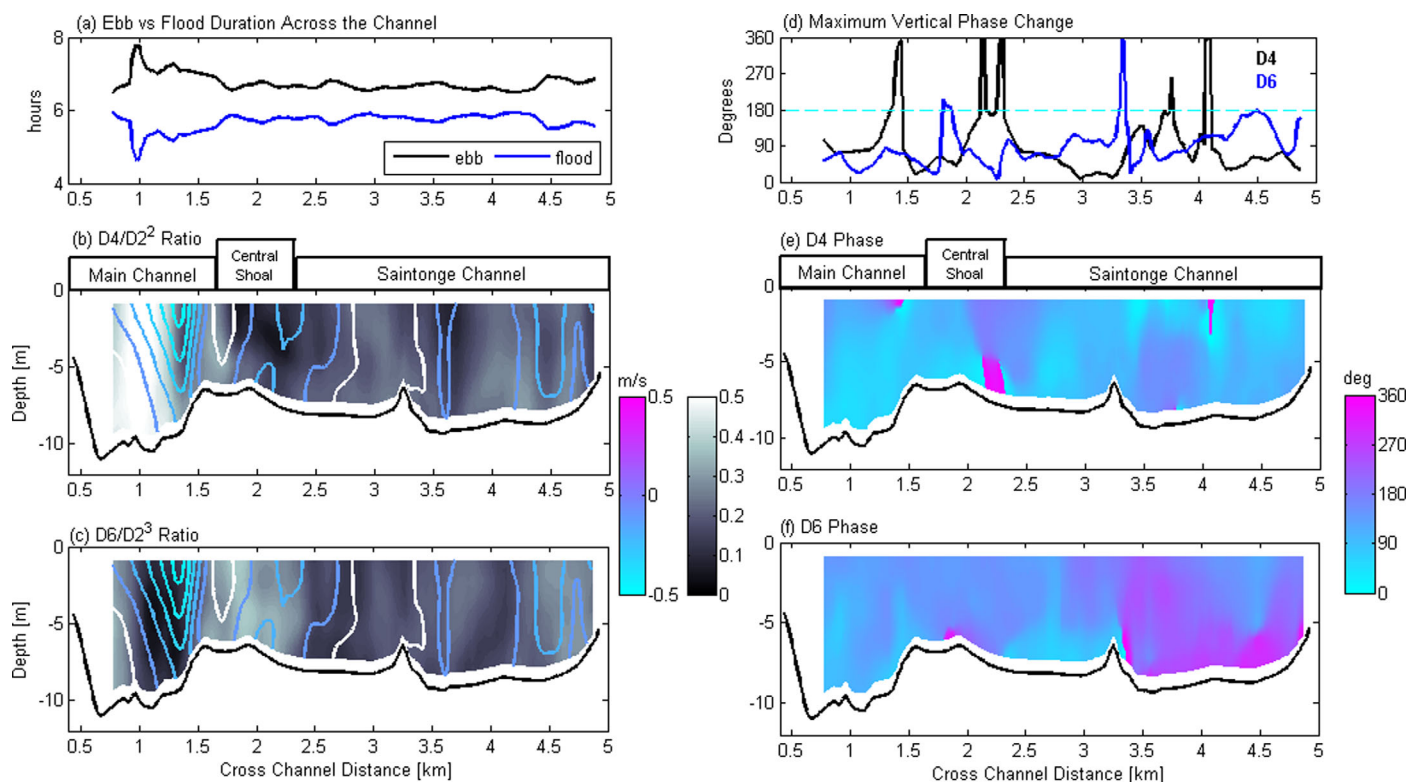


Figure 8. Same as Figure 6 but during spring tides.

throughout the water column (not shown). The residual (subtidal) flow was quantified at the mooring location for both the along and cross-channel velocities. The along-channel subtidal flow showed residual outflow throughout the water column reaching nearly 0.5 m/s at the surface. The cross-channel flow was directed westward, or toward the main channel, throughout the water column with velocities reaching ~ 0.2 m/s at the surface (Figure 9d). The ADCP transect data from neap tide shows largest $D4/D2^2$ ratios in locations of subtidal outflow (Figure 5b). The ADCP_m data verify these results as it also show elevated $D4/D2$ ratios where the subtidal flow is directed seaward (Figures 9b and 9d). The phase shift of $D4$ over the water column was found to be negligible in the ADCP_m data (not shown) indicating that internal tidal asymmetry is not the only generating mechanism for $D4$ during neap tide.

During spring tide there was an increase in tidal currents and tidal nonlinearities (Figure 9e). The amplitude of $D6$ was larger than $D4$ from the surface ($z/H=0$) to $z/H \sim -0.8$ where $D4$ then surpassed $D6$ (Figure 9f). In addition, the ratio of $D4/D2$ was comparable to that of $D6/D2$. The phase of $D4$ and $D6$ showed negligible phase change throughout the water column (not shown). Along-channel subtidal outflow reached ~ 0.6 m/s at the surface decreasing to ~ 0.1 m/s near bottom. The cross-channel subtidal flow reached ~ 0.1 m/s at the surface decreasing to ~ 0 m/s near bottom.

From the analysis of the ADCP transects and the ADCP_m moorings, it is clear that tidal nonlinearities influence subtidal dynamics at the mid-reaches of the Gironde. The neap tide ADCP transects indicate that internal asymmetries generate $D4$ at certain cross-channel locations. This was identified from a 180° phase shift of the $D4$ current amplitude over the water column (Figures 6d and 6e). No such phase shift was found in $D4$ in the ADCP_m data, indicating that internal asymmetry is not the only mechanism generating $D4$ during neap tide. To further examine the role of baroclinic effects, a Tidal Froude Number was used to compare tidal advective accelerations and baroclinicity as mechanisms generating the subtidal flow.

4.6. Tidal Froude Number

A Tidal Froude Number (Fr_o ; equation (4)) was first calculated across the estuary to determine the relative importance of baroclinic pressure gradients and tidal advective accelerations on the subtidal flow during

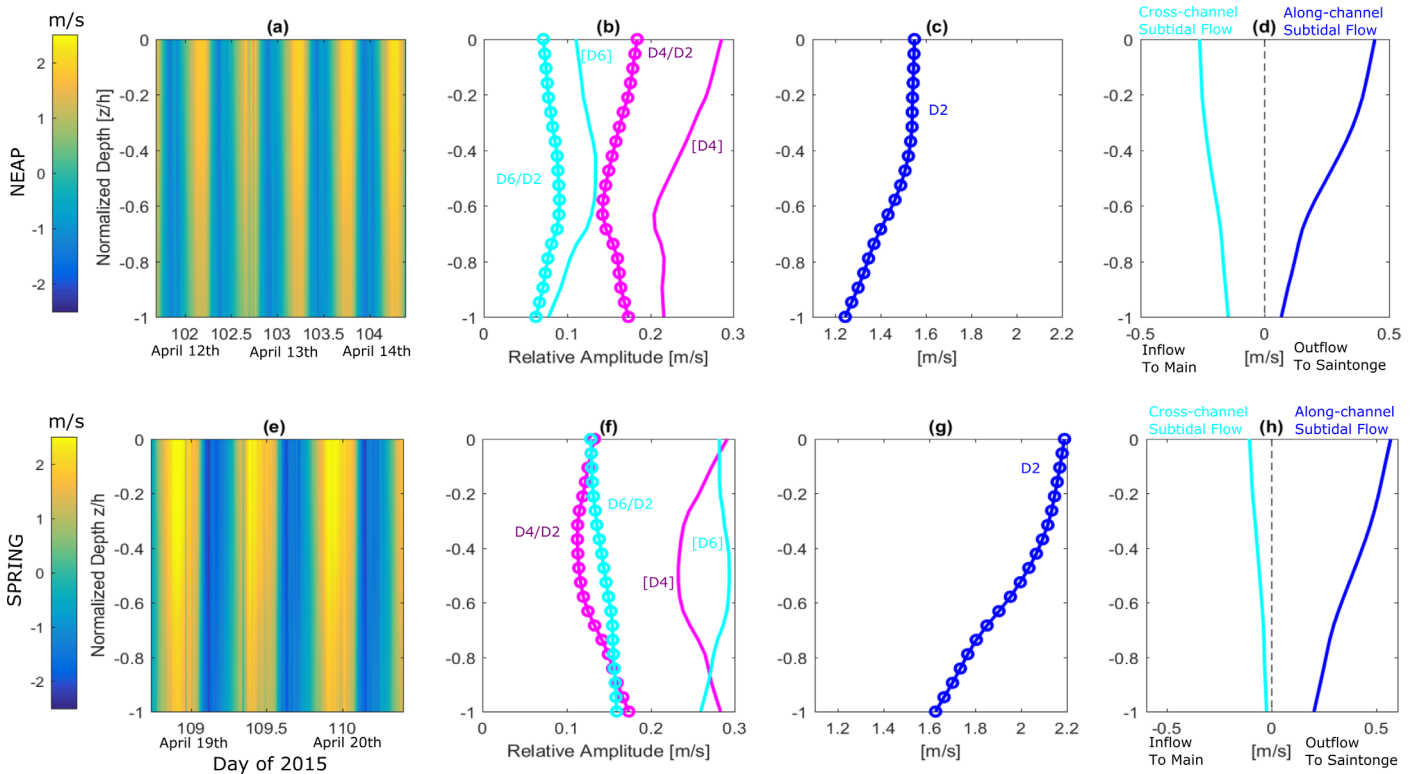


Figure 9. (a) ADCP_m along-channel velocity depicted with sigma coordinates ($z/H=0$ is the surface and $z/H=-1$ is the first ADCP bin above the bottom) during the neap tide sampling, (b) the D4 and D6 current velocity amplitude calculated using the least squares fit method and the ratios of D4 and D6 the D2 velocity amplitude. The units on the x axis for the amplitude of D4 and D6 are m/s and are shown in brackets, while the ratios D4/D2 and D6/D2 are given as relative amplitudes. (c) The D2 velocity amplitude. (d) The along-channel and cross-channel residual flow. (e–h) Same as Figures 9a–9d but for spring tide.

neap and spring tides. Remarkably, Fr_o values were almost identical during both neap and spring tides ($1.25 < \log_{10}(Fr_o) < 2$), suggesting that the influence of the advective accelerations versus baroclinicity does not change significantly throughout the spring/neap cycle (Figure 10a). This indicates that tidal advective accelerations are a driver of subtidal flow during both spring and neap tides. To further substantiate this claim, the Tidal Froude Number was calculated with the reduced gravity derived from vertical salinity profiles (Figures 10b–10d). This analysis also showed that tidal advective accelerations dominated over baroclinicity during spring and neap tides and will be explored further in the discussion section.

Both tidal advective accelerations and internal asymmetry have been found to generate subtidal flows, through the introduction of the D4 tidal species, during neap tides, with different mechanisms dominating across the estuary. Spring tide subtidal flows are also generated by advective accelerations. Quadratic friction is known to generate overtides in estuaries with strong tidal currents and has not yet been explored. Numerical model simulations with varying friction values will now be discussed to determine if quadratic friction also drives subtidal flows.

4.7. Model

Subtidal flow from the ADCP transects was compared to numerical model runs forced by rivers and tide conditions similar to those during data collection. The tidal range at Pauillac during the spring tide model run was 5 m (from -2 to 3 m; Figures 1 and 11e) and the river discharge prescribed was ~ 1300 m³/s, representing actual river discharge values on 20–21 April 2015 (spring tide measurement period for combined Garonne and Dordogne Rivers). Tidal range during the neap tide sampling was 3.5 m (from -1.25 to 2.25 m) at Pauillac (Figure 11f) and the river discharge value used in the model run was ~ 700 m³/s, or actual river discharge on 13–14 April 2015 (neap tide measurement period for combined Garonne and Dordogne Rivers).

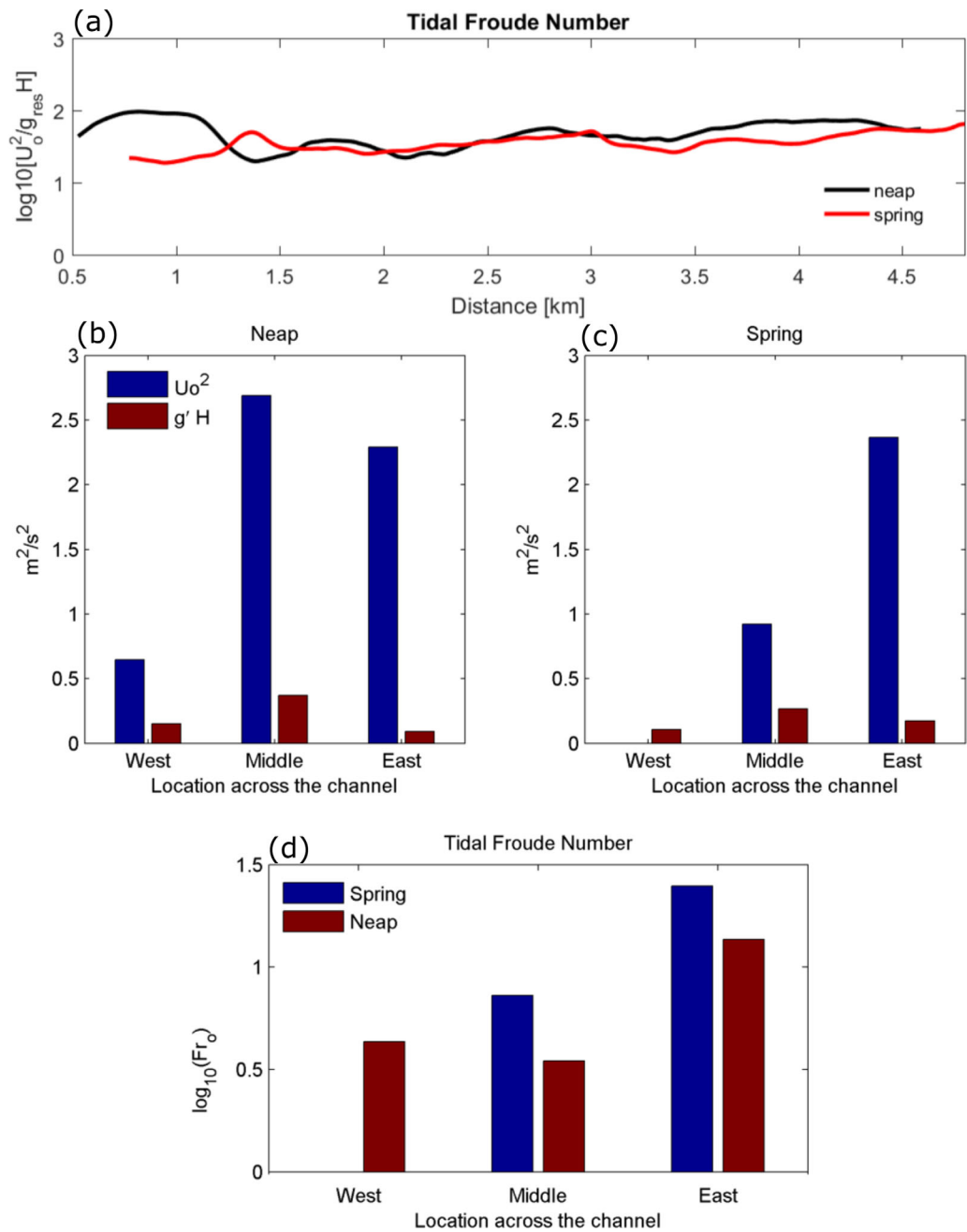


Figure 10. (a) Tidal Froude Number for neap and spring tide. Black line depicts neap tide, and the red line depicts spring tide. Results indicate that advection is almost 2 orders of magnitude greater than baroclinicity. The reduced gravity for Figure 10a was calculated from horizontal density contrasts. The main contributors to the Tidal Froude Number, U_0^2 (blue bars) and $(g'H)$ (red bars) at each of the three CTD profile locations (west, middle, and east) during (b) neap and (c) spring tides. The reduced gravity for Figures 10b and 10c was calculated with vertical salinity profiles. (d) Tidal Froude Number values at each of the CTD profile locations calculated with tidal advective accelerations, U_0^2 and baroclinicity, $(g'H)$ values from Figures 10b and 10c for both neap (red bars) and spring (blue bars) tides.

Subtidal flow and overtide amplitudes from the model simulations indicated that tidal nonlinearities drove subtidal flow (D4 and D6 overtide amplitudes >0.1 m/s for spring and neap tides), yet the model simulations underestimated subtidal flows when compared to data (Figures 5 and 11). In particular, model results showed subtidal outflow in the main channel, the central shoal (1.5–2.75 km) and in the Saintonge Channel (3.5–4.5 km) for both neap and spring tides (Figures 11a and 11c, respectively). Maximum subtidal flows for neap and spring tides occurred in the main channel reaching ~ 0.1 and ~ 0.3 m/s, respectively (Figures 11a and 11c).

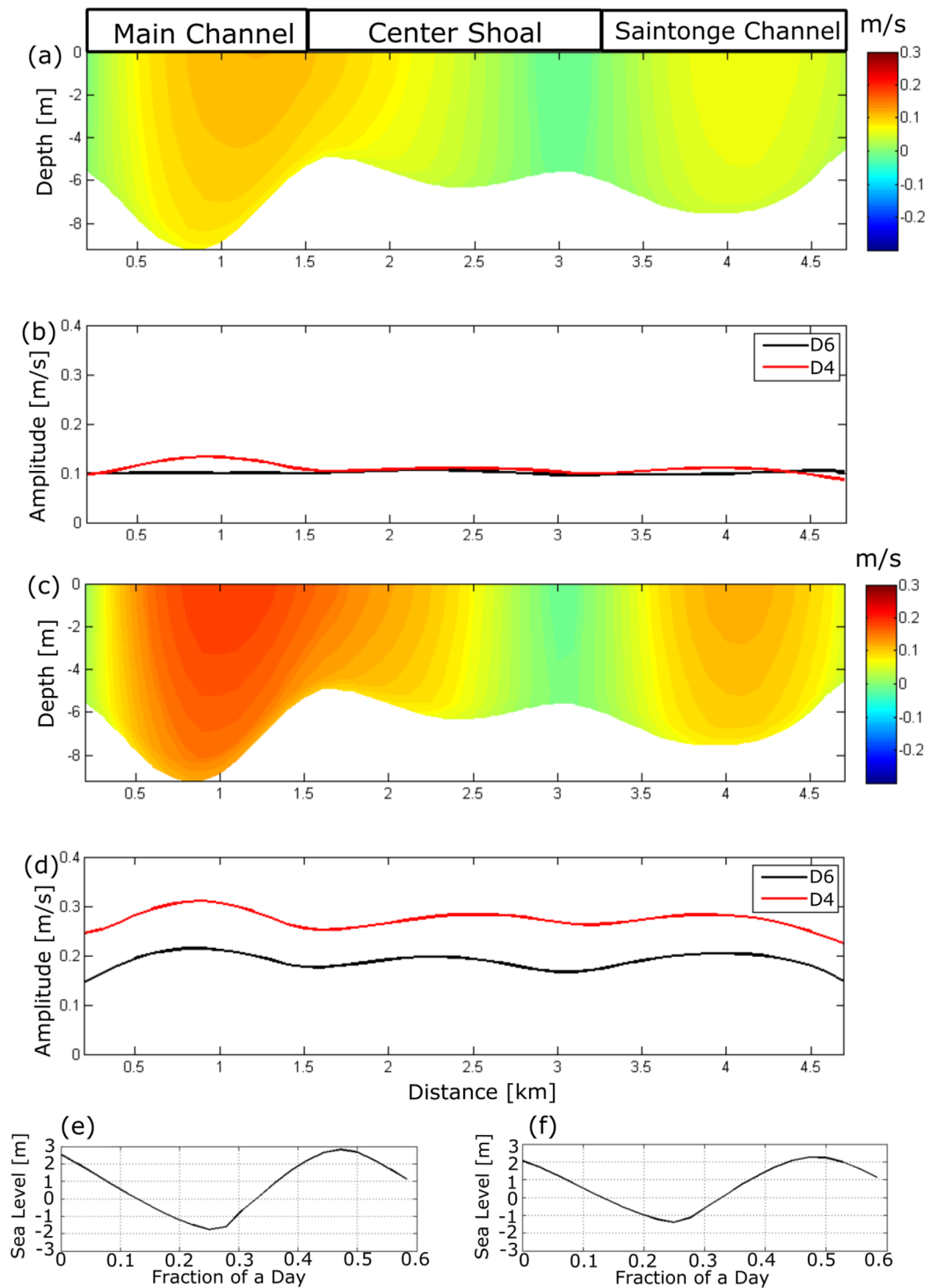


Figure 11. Results from the Telemac 3D numerical model simulation. Positive values depict outflow. (a) Along-channel residual flow during neap tide (m/s), (b) depth-averaged D4 (red line) and D6 (black line) current velocity amplitude during neap tide. (c and d) Same as Figures 11a and 11b but for spring tide. Tidal range during (e) spring and (f) neap tides.

Depth-averaged D4 and D6 current amplitudes were calculated from the neap and spring tide numerical experiments (Figures 11b and 11d, respectively). Amplitudes of both overtides were ~ 0.1 m/s for both D4 and D6 during neap tide (Figure 11b), and both increased (D4: ~ 0.27 m/s; D6: ~ 0.19 m/s) during spring tide (Figure 11d). The neap tide numerically simulated overtide amplitudes (D4 and D6) underestimated (by

~35%) the overtide amplitudes derived from the ADCP transect data (Table 1). During spring tide, the D4 amplitude from the model and the transect data were comparable (0.26 m/s from the data and 0.27 m/s from the model). However, the D6 amplitude was underestimated (24%) by the model simulation. These results imply that during neap tide there could be other nonlinear terms generating the subtidal flow and overtides other than quadratic friction and a mean flow (river). In fact, internal asymmetry was found to generate D4 during neap tide in the ADCP transect data, and as density gradients were not included in the model simulations, this could be the cause. Other factors that could contribute to this underestimation are model error through the friction coefficients, inaccurate model bathymetry, or spatial resolution. Further, some error could result from the short ADCP data set and/or ungaged river flow from small tributaries, or from wind-induced circulation. During spring tide, quadratic friction combined with mean flow can explain the D4 generation, but D6 must solely be caused by increasing quadratic friction. This will be explored further in section 5.

5. Discussion

The goals of this study are to determine if transverse distributions of tidal nonlinearities produce lateral variations of subtidal flow and to explore if this changes from neap to spring tides. Results showed that the intensity of tidal nonlinearities varied across the channel producing lateral variations of subtidal flow during both neap and spring tides. The following section will discuss the generating mechanisms of the overtide bands D4 and D6 and how they vary across the channel and from neap to spring tide.

5.1. Neap Tide

During neap tide, D4 was generated by internal asymmetry (Figures 6a, 6b, 6d, and 6e) and tidal advective accelerations (Figure 10). The estuary was flood dominant (longer duration ebb) and showed elevated $D4/D2^2$ ratios in cross-channel locations coinciding with subtidal outflow (Figures 6a and 6b). The ratio $D4/D2$ derived from water level measurements at Pauillac was small (0.031 during neap tide as opposed to 0.12 during spring tide) indicating that the D4 overtide in the current velocity was internally generated rather than barotropically generated in these cross-channel locations. The regions of flood dominance and elevated D4 amplitude were also a result of tidal advective accelerations.

During neap tide, internal asymmetry generated D4 in the current velocity, however, the Tidal Froude Number analysis indicated that advection was more influential than baroclinicity across the estuary. The limited spatial resolution (three stations) of the salinity and temperature profiles is a plausible explanation for why baroclinicity was not found to dominate in the cross-channel locations where internal asymmetries were shown to generate D4. The two analyses indicate that, during neap tides, both tidal advective accelerations and internal asymmetry generate D4 and subtidal flows at the mid-reaches of the Gironde.

The $D6/D2^3$ ratio was comparable to the $D4/D2^2$ ratio during neap tides (Figure 6 and Table 3). Quadratic friction is known to be the main contributor to D6 generation, yet when combined with river flow can also generate D4. However, as river flow increases, there is a subsequent decrease in D6 generation [Parker, 1991]. Alternately, a strong Stokes drift return flow could mimic river flow and produce D4 [Moftakhari et al., 2016]. To test whether this mechanism produced D4 in the Gironde, the Stokes drift transport was approximated in one dimension as $Q_{stokes} \approx 0.5U_{D2}Z_{D2}\cos(\phi_{UD2} - \phi_{ZD2})$ (following Moftakhari et al. [2016] adapted from Longuet-Higgins [1969]). Here Q_{stokes} is the Lagrangian Stokes drift, U_{D2} is the D2 tidal velocity amplitude, Z_{D2} is the D2 tidal height amplitude, ϕ_{UD2} is the phase of the tidal velocity, and ϕ_{ZD2} is the phase of the tidal height. It was found that Q_{stokes} never exceeded 0.1% of the river discharge (not shown), indicating that Stokes drift return flow was not responsible for generating D4 in the Gironde during neap or spring tide.

Table 3. Sectional Mean of Depth-Averaged D4 and D6 Velocity Amplitude for Neap and Spring Tides

Harmonic	Sectional Mean (Transects) (m/s)		Depth Averaged (Mooring) (m/s)	
	Neap	Spring	Neap	Spring
D2	1.24	1.16	1.45	1.97
D4	0.15	0.26	0.24	0.26
D6	0.16	0.25	0.12	0.28

5.2. Spring Tide

The nonlinear mechanisms driving overtide generation and subtidal flow changed from neap to spring tide. River discharge values were higher during the spring tide measurement period (~600 m³/s greater than neap

tide), resulting in flood dominance across the estuary (Figure 8a) and stronger subtidal outflow than neap tide (Figures 2, 5, and 7). This was verified by a depth average of the subtidal flow (Figure 12a) and was expected due to the flood dominance across the estuary width (Figure 8a), larger river discharge (Figure 2a) and Tidal Froude Number indicating that tidal advective accelerations dominated over baroclinicity (Figures 10). Therefore, D4 was generated by advective accelerations rather than baroclinicity. Further, phase shifts of D4 were scarcely 180° (only in the Saintonge Channel between 4.25 and 4.7 km and in the Central Shoal at 1.75 km) and did not correspond to elevated D4/D2² ratios. This indicates that internal asymmetry did not generate D4 during spring tides, as would be expected due to increased tidal mixing.

Both D4 and D6 were larger during spring tides than neap but remained comparable (~ 0.25 m/s) (Figures 12b and 12c and Table 3). Stronger tidal velocities during spring tide increased quadratic friction and hence elevated the D6 amplitude (Figure 12c). However, river discharge was higher during spring tide than neap,

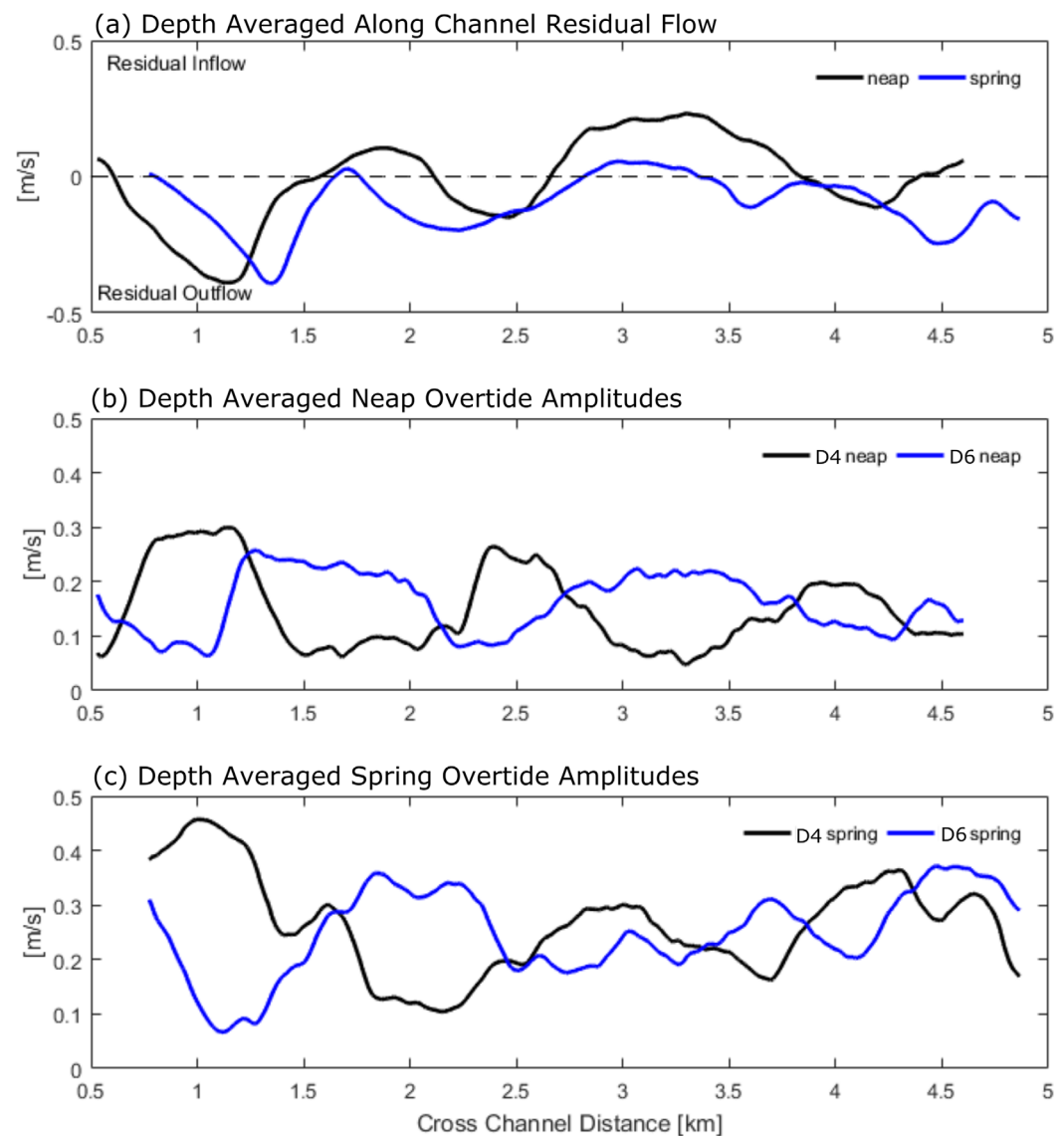


Figure 12. (a) Depth-averaged residual flow from measurements for neap and spring tides (cm/s) with respect to cross-channel location (x axis). The black line depicts results from neap tide and the blue line depicts results from spring tide. Negative values denote outflow and positive values denote inflow. (b) The depth-averaged D4 (black line) and D6 (blue line) amplitudes for neap tide with respect to cross-channel location. (c) Same as Figure 12b but for spring tide.

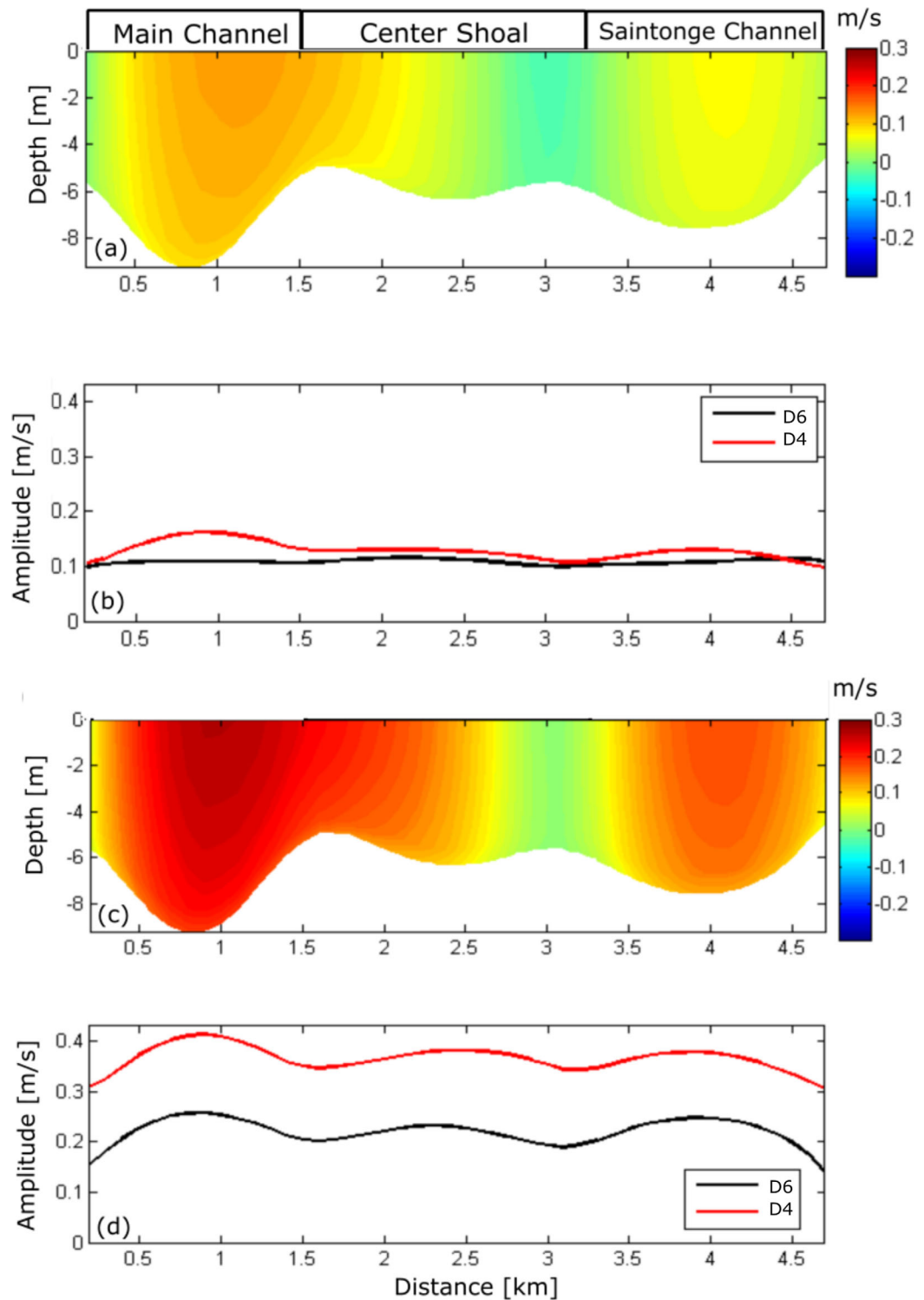


Figure 13. Results from the Telemac 3D numerical model simulation with reduced friction values along the estuary. Positive values depict outflow. (a) Along-channel residual flow during neap tide (m/s), (b) depth-averaged D4 (red line) and D6 (black line) current velocity amplitude during neap tide. (c and d) Same as Figures 13a and 13b but for spring tide. This figure shows that reduced friction strengthens residual flow and increases the amplitude of D4 during spring tides.

indicating that D4 could also be generated by the combination of quadratic friction and mean flow. In addition, the D4/D2 ratio derived from the water level during spring tide was 0.12 indicating that D4 could be generated by barotropic nonlinearities derived from the terms $\partial(\zeta u)/\partial x$ and $\zeta u|u|$.

In summary, during spring tides, D4 was likely generated by a combination of tidal advective accelerations (found through an elevated Tidal Froude Number) and water level variations (found from flood dominance of the estuary, Figure 8a). Although the influence of quadratic friction combined with mean flow could also contribute to D4 during spring tides, this was not quantifiable with the current data set. The D6 amplitude increased from neap to spring tide due to increased quadratic friction, but remained comparable to D4. The role of friction on D4 and D6 generation is explored further with numerical simulations.

5.3. Spring/Neap Variation in Subtidal Flow

A numerical experiment was performed with prescribed reduced friction in the Telemac model (Figure 13). The goal was to determine how changing bottom friction would alter the subtidal flow pattern and D4 and D6 amplitudes. The Strickler Bottom Friction coefficient (which is a reciprocal of Manning's n) was reduced by a constant value of 10 along the estuary. Results showed that reducing friction allowed for larger subtidal flows (than the case with increased friction, Figure 11) and for D4 to exceed D6 during spring tide (D4: ~ 0.35 m/s; D6: ~ 0.2 m/s; Figure 13b). This implied that increased friction allowed more transfer of nonlinearities to the D6 and less to the residual flows during spring tide. The strong influence of the D6 harmonic has been documented in literature, but the analyses are limited to time series analysis or along-channel variations of the D6 overtide rather than cross-channel [Godin, 1999; Blanton *et al.*, 2002; Gallo and Vinzon, 2005; Valle-Levinson *et al.*, 2007].

This study revealed that the D6 overtide band was comparable to D4 during neap and spring tides in a macrotidal estuary (Figure 12). In portions of the estuarine cross-section where density gradients were strong, internal asymmetry generated the D4 harmonic and the subtidal flow was reinforced (Figure 6). During neap tide, river discharge was relatively small for the Gironde and density gradients contributed to the subtidal flows producing cross-channel sections of subtidal inflow and outflow. In turn, when river discharge increased during spring tides, density stratification migrated downstream of the sampling site. Therefore, baroclinic pressure gradients could take on a more prominent role in the subtidal flow dynamics downstream. This downstream shift in baroclinicity explains why internal asymmetries were not found in D4 during spring tide and rather, subtidal outflow was prominent across the channel. This work implies that tidal nonlinearities and their effects on subtidal flow can vary across estuary and have fortnightly temporal variability.

The cross-channel variation of overtides, such as D4 and D6, should be considered in more detail in relation to sediment transport in the Gironde and other similar systems. In particular, the Gironde is known for its well-developed turbidity maximum zone and exceptionally complex sediment dynamics [Sottolichio *et al.*, 2011]. Flood dominance in estuaries, and hence tidal asymmetries, cause sediment transport and deposition inside the basin [Allen *et al.*, 1980; Friedrichs and Aubrey, 1988; Blanton *et al.*, 2002]. Ridderinkhof [1997] found that D6 can influence bed load and suspended load transport when the net transport due to D2 interacting with D4 is negligible. But it remains that the links between sediment trapping and higher overtides like D6 [Ridderinkhof, 1997] and cross-channel variations in D4 have not been studied extensively and warrant further investigation.

6. Conclusions

Lateral variability of tidal nonlinearities and subtidal flow was investigated at the mid-reaches of the Gironde Estuary. Transverse distributions of tidal nonlinearities (quarter-diurnal and sixth-diurnal bands) were found to produce lateral variations of subtidal flows during neap and spring tides. During neap tide, subtidal flow was laterally sheared at multiple locations across the estuary while subtidal outflow dominated during spring tide. During neap tide, elevated D4/D2² ratios were found in cross-channel locations of subtidal outflow and flood dominance, which was found to be generated by internal asymmetry and tidal advective accelerations. The sixth-diurnal harmonic band (D6) was found in regions of subtidal inflow and where D4/D2² ratios were negligible, indicating that in these cross-channel locations energy was transferred from D2 to D6 by quadratic friction. During spring tide, both river discharge and tidal currents increased, subtidal flows were directed out-estuary throughout the estuarine cross-section and overtide amplitudes increased relative to neap tide. Internal asymmetry did not generate D4 due to the increased tidal currents in spring tides. Rather, tidal advective accelerations and water level variations generated D4. The D6 amplitude was comparable to D4 during spring tide and was largest in areas of negligible subtidal flow (same as

neap tide). This was attributed to increased tidal flows producing enhanced quadratic friction and hence generating D6. This study reveals that cross-channel variations of tidal nonlinearities in a macrotidal estuary can affect the lateral structure of subtidal flow, and that this influence differs from neap to spring tides. Further studies will include lateral variability of subtidal flow at locations further downstream in order to determine whether forcing mechanisms change longitudinally in the estuary.

Acknowledgments

We would like to thank Mario Lepage (IRSTEA) and Guillaume Detandt (EPOC) for helping with the data collection. We also thank Énergie de la Lune (EDL) for aiding in the collection of the moored ADCP data. We gratefully acknowledge the financial support of the URABAILA BPI Project. This project is a contribution to the CNRS observation program DYNALIT. Arnoldo Valle-Levinson acknowledges support from US NSF project OCE 1332718. The authors would like to thank one anonymous reviewer and Stefan Talke for their invaluable comments and suggestions. The data used in this study are available at the following link: <http://dataverse.acg.maine.edu/dvn/faces/study/Study-Page.xhtml?globalId=hdl:TEST/10137>.

References

- Allen, G. P., and P. Castaing (1973), Suspended sediment transport from the Gironde estuary (France) onto the adjacent continental shelf, *Mar. Geol.*, *14*, M47–M53.
- Allen, G. P., J. C. Salomon, P. Bassoullet, Y. Du Penhoat, and C. De Grandpré (1980), Effects of tides on mixing and suspended sediment transport in macrotidal estuaries, *Sediment. Geol.*, *26*, 69–90.
- Aubrey, D. G., and P. E. Speer (1985), A study of non-linear tidal propagation in shallow inlet/estuarine systems, Part I: Observations, *Estuarine Coastal Shelf Sci.*, *21*, 185–205.
- Becker, M., and C. Winter (2016), Sediment-induced stratification and density current in the Ems estuary, paper presented at Physics of Estuaries and Coastal Seas (PECS) Conference, Delft, The Netherlands, 9–14 Oct.
- Blanton, J. O., G. Lin, and S. A. Elston (2002), Tidal current asymmetry in shallow estuaries and tidal creeks, *Cont. Shelf Res.*, *22*, 1731–1743.
- Bonneton, P., N. Bonneton, J. P. Parisot, and B. Castelle (2015), Tidal bore dynamics in funnel-shaped estuaries, *J. Geophys. Res. Oceans*, *120*, 923–941, doi:10.1002/2014JC010267.
- Brown, J. M., and A. G. Davies (2010), Flood/ebb tidal asymmetry in a shallow sandy estuary and the impact on net sand transport, *Geomorphology*, *114*(3), 431–439.
- Dronkers, J. (1986), Tidal asymmetry and estuarine morphology, *Neth. J. Sea Res.*, *20*, 117–131.
- Dyer, K. R. (1973), *Estuaries: A Physical Introduction*, John Wiley, New York.
- Dyer, K. R. (1986), *Coastal and Estuarine Sediment Dynamics*, John Wiley, New York.
- Emery, W. J., and R. E. Thomson (2001), *Data Analysis Methods in Physical Oceanography*, Elsevier, Amsterdam, The Netherlands.
- Foreman, M. G. G. (1977), Manual for tidal heights analysis and prediction, *Pac. Mar. Sci. Rep.* 77–10, Inst. of Ocean Sci., Sidney, British Columbia, Australia.
- Friedrichs, C. T., and D. G. Aubrey (1988), Non-linear tidal distortion in shallow well-mixed estuaries: A synthesis, *Estuarine Coastal Shelf Sci.*, *27*, 521–545.
- Gallo, M. N. and S. B. Vinzon (2005), Generation of overtides and compound tides in Amazon estuary, *Ocean Dyn.*, *55*, 441–448, doi:10.1007/s10236-005-0003-8.
- George, K. J., and B. Simon (1984), The species concordance method of tide prediction in estuaries, *Internal Hydrogr. Rev.*, *LXI* 1, 121–146.
- Geyer, R. W. (1993), The importance of suppression of turbulence by stratification on the estuarine turbidity maximum, *Estuaries*, *16*(1), 113–125.
- Gibbs, R. J., D. M. Tshudy, L. Konwar, and J. M. Marin (1989), Coagulation and transport of sediments in the Gironde Estuary, *Sedimentology*, *36*, 987–999.
- Godin, G. (1999), The propagation of tides up rivers with special considerations on the upper Saint Lawrence River, *Estuarine Coastal Shelf Sci.*, *48*, 307–324.
- Huijts, K. M. H., H. M. Schuttelaars, H. E. de Swart, and C. T. Friedrichs (2009), Analytical study of the transverse distribution of along-channel and transverse residual flows in tidal estuaries, *Cont. Shelf Res.*, *29*, 89–100.
- Huybrechts, N., C. Villaret, and F. Lyard (2012), Optimized predictive two-dimensional hydrodynamic model of the Gironde estuary in France, *J. Waterw. Port Coastal Ocean Eng.*, *138*, 312–322.
- Jalón-Rojas, I., S. Schmidt, and A. Sottolichio (2015), Turbidity in the fluvial Gironde Estuary (southwest France) based on 10-year continuous monitoring: Sensitivity to hydrological conditions, *Hydro. Earth Syst. Sci.*, *19*, 2805–2819, doi:10.5194/hess-19-2805-2015.
- Jay, D. A. (1991), Internal asymmetry and anharmonicity in estuarine flow, in *Tidal Hydrodynamics*, edited by B. Parker, pp. 521–543, John Wiley, New York, N. Y.
- Jay, D. A., and T. Kukulka (2003), Revising the paradigm of tidal analysis—The uses of non-stationary data, *Ocean Dyn.*, *53*, 110–125.
- Jay, D. A., and J. D. Musiak (1996), Internal tidal asymmetry in channel flows: Origins and consequences, in *Mixing Processes in Estuaries and Coastal Seas, Coastal Estuarine Sci. Monogr. Ser.*, edited by C. Pattiaratchi, pp. 219–258, AGU, Washington, D. C.
- Joyce, T. M. (1989), On in situ "calibration" of shipboard ADCPs, *J. Atmos. Oceanic Technol.*, *6*, 169–172.
- Le Hir, P., P. Bassoullet, and H. Jestin (2000), Application of the continuous modelling concept to simulate high-concentration suspended sediment in a macrotidal estuary. in *Coastal and Estuarine Fine Sediments Processes*, edited by W. H. McAnally and A. J. Mehta, pp. 229–247, Elsevier, Amsterdam.
- Longuet-Higgins, M. S. (1969), On the transport of mass by time-varying ocean currents, *Deep Sea Res. Oceanogr. Abstr.*, *16*, 431–447.
- Lwiza, K. M. M., D. G. Bowers, J. H. Simpson (1991), Residual and tidal flow at a tidal mixing front in the North Sea, *Cont. Shelf Res.*, *11*(11), 1379–1395.
- Moftakhari, H. R., D. A. Jay, and S. A. Talke (2016), Estimating river discharge using multiple-tide gauges distributed along a channel, *J. Geophys. Res. Oceans*, *121*, 2078–2097, doi:10.1002/2015JC010983.
- Parker, B. B. (1991), The relative importance of the various nonlinear mechanisms in a wide range of tidal interactions (review), in *Tidal Hydrodynamics*, edited by B. Parker, pp. 237–268, John Wiley, New York, N. Y.
- Prandle, D. (1991), Tides in estuaries and embayments (review), in *Tidal Hydrodynamics*, edited by B. Parker, pp. 237–268, John Wiley, New York.
- RD Instruments (1999), Measuring river discharge in high flow (Flood) or high sediment concentration conditions, *Appl. Note FSA-007*, pp. 1–4, Poway, Calif.
- Ridderinkhof, H. (1997), The effect of tidal asymmetries on the net transport of sediments in the Ems Dollard Estuary, *J. Coastal Res.*, *25*, 41–48.
- Ross, L., and A. Sottolichio (2016), Subtidal variability of sea level in a macrotidal and convergent estuary, *Cont. Shelf Res.*, *131*, 28–41.
- Salomon, J. C., and G. Allen (1983), Role sedimentologique de la maree dans les estuaires a fort marnage, *Compagnie Francais des Petroles, Notes Memo.*, *18*, 35–44.
- Simpson, J. H., J. Sharples, T. P. Rippeth (1991), A prescriptive model of stratification induced by freshwater runoff, *Estuar. Coast. Shelf Sci.*, *33*, 23–35.

- Sottolichio, A. (1999), Modeling dynamics of turbidity maximum and fluid mud in the Gironde estuary, PhD thesis, n° 2061, 190 pp., Univ. of Bordeaux I, Bordeaux, France.
- Sottolichio, A., and P. Castaing (1999), A synthesis on seasonal dynamics of highly concentrated structures in the Gironde estuary, *C. R. Acad. Sci., Ser. II*, 329, 795–800.
- Sottolichio, A., D. Hurther, N. Gratiot, and P. Breitel (2011), Acoustic turbulence measurements of near-bed suspended sediment dynamics in highly turbid waters of a macrotidal estuary, *Cont. Shelf Res.*, 31, S36–S49.
- Speer, P. E., and D. G. Aubrey (1985), A study of non-linear tidal propagation in shallow inlet/estuarine systems, Part II: Theory, *Estuarine Coastal Shelf Sci.*, 21, 207–224.
- Talke, S. A., H. E. de Swart, and H. M. Schuttelaars (2009), Feedback between residual circulations and sediment distribution in highly turbid estuaries: An analytical model, *Cont. Shelf Res.*, 29(1), 119–135.
- Tee, K. T. (1976), Tide-induced residual current, a 2-D nonlinear numerical model, *J. Mar. Res.*, 34(4), 603–628.
- Uncles, R. J. (1981), A note on tidal asymmetry in the Severn Estuary, *Estuarine Coastal Shelf Sci.*, 13, 419–432.
- Valle-Levinson, A. and K. M. M. Lwiza (1995), Effects of channels and shoals on the exchange between the lower Chesapeake Bay and the adjacent ocean, *J. Geophys. Res.*, 100(C9), 18, 551–563.
- Valle-Levinson, A., and C. A. Schettini (2016), Fortnightly switching of residual flow drivers in a tropical semiarid estuary, *Estuarine Coastal Shelf Sci.*, 169, 46–55, doi:10.1016/j.ecss.2015.12.008.
- Yorozuya, A., Y. Motonaga, Y. Iwami, T. Furuyama, and K. Ogiwara (2014), Water discharge measurements with ADCP in high speed flow with high sediment concentration, paper presented at 9th International Symposium on Ultrasonic Doppler Methods for Fluid Mechanics and Fluid Engineering, 27–29 Aug, 2014, Strasbourg, France.